

Transformer-Based Neural Quantum Digital Twins for Many-Body Quantum Simulation and Optimal Annealing Schedule Design

Jianlong Lu,^{1,*} Hanqiu Peng,^{1,*} and Ying Chen^{1,2,3,†}

¹*Department of Mathematics, Faculty of Science, National University of Singapore*

²*Centre for Quantitative Finance, Faculty of Science, National University of Singapore*

³*Risk Management Institute, National University of Singapore*

(Dated: December 23, 2025)

Abstract

We introduce Transformer-based Neural Quantum Digital Twins (Tx-NQDTs) to simulate full adiabatic dynamics of many-body quantum systems, including ground and low-lying excited states, at low computational cost. Tx-NQDTs employ a graph-informed Transformer neural network trained to predict spectral properties (energy levels and gap locations) needed for annealing schedule design. We integrate these predictions with an adaptive annealing schedule design based on first-order adiabatic perturbation theory (FOAPT), which slows the evolution near predicted small gaps to maintain adiabaticity. Experiments on a D-Wave quantum annealer ($N = 10, 15, 20$ qubits, 12 control segments) show that Tx-NQDT-informed schedules significantly improve success probabilities despite hardware noise and calibration drift. The optimized schedules achieve success probabilities 2.2–11.7 percentage points higher than the default linear schedule, outperforming the D-Wave baseline in 44 of 60 cases. These results demonstrate a practical, data-driven route to improved quantum annealing performance on real hardware.

1. INTRODUCTION

Quantum annealing provides a hardware-efficient approach to solving combinatorial optimization problems, particularly quadratic unconstrained binary optimization (QUBO), by exploiting adiabatic evolution under time-dependent Hamiltonians [1–3]. In a quantum annealing process, the system is initialized in the ground state of a simple driver Hamiltonian and is evolved continuously along an anneal path toward a problem Hamiltonian whose ground state encodes the desired solution. In the ideal adiabatic limit, sufficiently slow evolution guarantees that the system remains in its instantaneous ground state throughout the anneal.

In practical devices, however, anneals are necessarily finite in duration. As a result, nonadiabatic transitions occur, especially near points along the anneal path where the spectral gap between the ground state and low-lying excited states becomes small. These narrow-gap regions govern annealing performance: the evolution must slow down locally to suppress diabatic excitations, while in wide-gap regions the system can safely evolve faster. Designing annealing schedules that adapt to this highly nonuniform spectral structure is therefore central to achieving high success probabilities.

Commercial quantum annealers developed by e.g. D-Wave, Fujitsu, Qilimanjaro, and NEC have enabled exploratory applications in finance, logistics, and materials science, while requiring fewer high-fidelity gate operations and offering partial robustness to certain noise

sources [4]. Nonetheless, empirical performance remains problem-dependent and is critically influenced by the annealing schedule [5, 6]. Current hardware implementations largely rely on fixed or weakly parameterized schedules, despite mounting evidence that instance-specific, adaptive schedules can substantially improve outcomes.

This leads to a central challenge: *how can one determine annealing rates along the anneal path that balance computational efficiency with solution fidelity?* Addressing this question requires access to the instantaneous spectral structure – ground-state energy, low-lying excited states, and energy gaps – along the full time-dependent evolution. However, present-day quantum annealers cannot directly measure these quantities during execution [7]. As a result, effective schedule design depends on accurate classical surrogates capable of tracking spectral evolution under time-dependent Hamiltonians.

Existing classical simulation methods each capture parts of this problem but fall short as general-purpose digital twins. Quantum Monte Carlo methods provide unbiased estimates for stochastic systems but become costly when repeatedly evaluating spectra along an anneal path and are hindered by the sign problem in more general settings [8–10]. Tensor network approaches are powerful for low-entanglement or quasi-one-dimensional systems, yet their computational cost grows rapidly for higher-dimensional or time-dependent problems [11, 12]. Dynamical mean-field theory captures local correlations but is not naturally suited to sparse QUBO or Ising coupling graphs, nor to resolving low-lying spectra across many anneal points [13]. Crucially, none of these approaches offers a spectrum-aware surrogate that is simultaneously accurate, graph-aware, and inexpensive enough to be used on a per-instance basis for schedule synthesis.

* These authors contributed equally to this work.

† Corresponding author: matcheny@nus.edu.sg

Neural network quantum states provide a promising alternative by offering expressive variational representations with favorable scaling properties [14–16]. Recent advances have demonstrated their ability to represent time-evolving states and transfer knowledge across related quantum problems [17–19]. However, most existing approaches focus on static ground states or short-time dynamics. Accurately simulating *full adiabatic evolution under time-dependent Hamiltonians*, including low-lying excited states along the entire anneal path, remains computationally demanding and largely unexplored.

In this work, we introduce a *Transformer-based Neural Quantum Digital Twin* (Tx-NQDT) designed specifically to model adiabatic dynamics along an annealing path. The model is explicitly aligned with the problem’s coupling graph and is trained to track ground and low-lying excited states as the anneal parameters vary in time. Tx-NQDT combines a graph-aware local-attention transformer with variance-controlled variational Monte Carlo and a deflation-based strategy for excited states, together with temporal transfer learning that propagates information smoothly along the anneal path. This design enables accurate reconstruction of instance-specific spectral structure at a computational cost suitable for schedule optimization.

The learned digital twin provides direct access to quantities that govern adiabatic performance – energy gaps and nonadiabatic couplings – which we use to construct adaptive annealing schedules based on first-order adiabatic perturbation theory. Importantly, this approach respects realistic hardware constraints. On D-Wave systems, annealing schedules can be modified using at most 12 programmable control segments, imposing a strict discretization and slope limit. We show that even under these constraints, Tx-NQDT-informed schedules systematically outperform standard linear schedules.

We validate the framework on transverse-field Ising models at small N (Appendix G) and evaluate random Hamiltonian instances at problem sizes of 10, 15, and 20 qubits, explicitly distinguishing between easy and hard instances based on minimum spectral gaps. For the random-Hamiltonian benchmarks, Tx-NQDT accurately captures gap profiles along the anneal path. Experiments on a D-Wave quantum annealer demonstrate consistent empirical gains despite calibration drift and device noise: optimized schedules improve success probabilities in 44 out of 60 tested instances, with particularly strong improvements on hard problems.

Together, these results show that neural quantum digital twins can serve as practical, spectrum-aware surrogates for time-dependent quantum dynamics, enabling adaptive control strategies that narrow the gap between ideal adiabatic evolution and noisy hardware execution.

The remainder of this paper is structured as follows: Section 2 introduces the Tx-NQDT architecture and training methodology; Section 3 details numerical experiments validating our spectral reconstruction accuracy; Section 4 demonstrates practical improvements in an-

nealing schedule optimization; and Section 5 discusses implications, limitations, and future research directions.

2. METHODOLOGY

This section outlines our methodological framework for constructing a Transformer-based Neural Quantum Digital Twin (Tx-NQDT) to simulate the adiabatic evolution of quantum many-body systems under a time-dependent annealing Hamiltonian. The goal is to approximate instantaneous eigenstates and energies along the full anneal path, rather than only static ground states at fixed Hamiltonian parameters.

2.1. QUBO and Time-Dependent Hamiltonians

We formulate the quadratic unconstrained binary optimization (QUBO) problem within the quantum-annealing framework and make explicit the time-dependent Hamiltonian that our Tx-NQDT must track.

QUBO instance specifies a real symmetric matrix $Q \in \mathbb{R}^{n \times n}$ and seeks

$$\min_{\mathbf{x} \in \{0,1\}^n} f_Q(\mathbf{x}) = \mathbf{x}^\top Q \mathbf{x}, \quad (1)$$

where Q encodes linear and quadratic coefficients of the objective [20]. Due to their generality, QUBO formulations can encode a wide range of NP-hard problems, including multi-dimensional subset-sum, low autocorrelation binary sequences, minimum Birkhoff decomposition, Steiner tree packing in graphs (VLSI design/wire routing), sports tournament scheduling (STS), and multi-period portfolio optimization with transaction costs [21, 22]. For annealing hardware it is more convenient to work with Ising variables $z_i \in \{-1, +1\}$. The two forms are related by an affine change of variables, so we work interchangeably with QUBO and Ising below.

Quantum annealing maps the classical objective to the ground state of a problem (final) Hamiltonian

$$H_P = \frac{1}{2} \left(\sum_i h_i \hat{\sigma}_z^{(i)} + \sum_{i>j} J_{ij} \hat{\sigma}_z^{(i)} \hat{\sigma}_z^{(j)} \right), \quad (2)$$

where $h_i \in \mathbb{R}$ are local fields that bias spins along $\pm z$, and $J_{ij} \in \mathbb{R}$ are couplings that favor correlated or anti-correlated spin assignments [23, 24]. The constants h_i, J_{ij} are exactly the quantities produced when the QUBO matrix is embedded on the hardware graph. They are also the inputs that our Tx-NQDT consumes.

The anneal starts from the easily prepared ground state of a transverse-field driver

$$H_0 = -\frac{1}{2} \sum_i \hat{\sigma}_x^{(i)}, \quad (3)$$

which introduces quantum fluctuations that delocalize the state over the computational basis. The system is

then evolved under a time-dependent Hamiltonian of the standard form

$$H(t) = A(t)H_0 + B(t)H_P, \quad t \in [0, T], \quad (4)$$

with boundary conditions $A(0) > 0$, $B(0) = 0$, $A(T) = 0$, $B(T) > 0$. It is often more convenient to reparameterize time by the dimensionless anneal parameter $s \in [0, 1]$, $s = t/T$, and write

$$H_{QA}(s) = A(s)H_0 + B(s)H_P. \quad (5)$$

This is the exact form used by our digital twin.

In the ideal adiabatic limit, if $A(s), B(s)$ change slowly enough and the instantaneous spectral gap between the ground state and the first excited state remains nonzero, the system follows the instantaneous ground state of $H_{QA}(s)$ for all s and ends in the optimal solution [25, 26]. Additional details are provided in Appendix A. On real hardware, however, T is finite and the gap $\Delta(s)$ may become small or highly localized in s , so diabatic transitions occur precisely where $A(s)$ and $B(s)$ should slow down or pause. Determining where these small-gap regions are, and how much to slow down there, is what motivates building a high-fidelity surrogate of the spectral evolution.

Notation. We use $s \in [0, 1]$ for the reduced anneal parameter and t for physical time. The schedule coefficients are $A(s)$ and $B(s)$. The lowest two energy levels of $H_{QA}(s)$ are denoted $E_0(s)$ and $E_1(s)$, with instantaneous gap $\Delta(s) = E_1(s) - E_0(s)$. The corresponding (normalized) eigenstates are $\Psi_0(s)$ and $\Psi_1(s)$, which we represent in the computational (Ising) basis as wavefunctions $\Psi_k(x; s)$ over spin configurations x . We write these wavefunctions in amplitude-phase form $\Psi_k(x; s) = \exp\{\log |\Psi_k(x; s)| + i\Phi_k(x; s)\}$ for generality. The quantity $\Lambda(s)$ denotes the adiabatic control functional (defined later in Sec. 2.4) which will guide our schedule optimization.

2.2. Transformer-based Neural Quantum Digital Twins

Accordingly, in what follows we (i) keep the physically standard $H_{QA}(s)$ above so we stay compatible with D-Wave-style schedules, but (ii) allow $A(s), B(s)$ to be supplied by an optimized schedule rather than a fixed catalog curve, and (iii) train a Tx-NQDT to output per-instance quantities such as $E_0(s)$, $E_1(s)$, and transition matrix elements $\langle \Psi_0(s) | \frac{dH_{QA}}{ds} | \Psi_1(s) \rangle$ that are needed later by FOAPT-style control functionals. This closes the loop between the abstract QUBO model, the hardware-compatible Hamiltonian, and the learning-based schedule synthesis described in Sec. 2.4.

We parameterize the variational wavefunction with a transformer neural network that is explicitly aligned with

the Ising/QUBO Hamiltonian

$$H_{QA}(s) = -\frac{A(s)}{2} \sum_i \hat{\sigma}_x^{(i)} + \frac{B(s)}{2} \left(\sum_i h_i \hat{\sigma}_z^{(i)} + \sum_{i>j} J_{ij} \hat{\sigma}_z^{(i)} \hat{\sigma}_z^{(j)} \right). \quad (6)$$

Here $s \in [0, 1]$ is the anneal parameter and $A(s), B(s)$ are the instantaneous schedule coefficients. The key idea is to make the network see exactly the same structural information as the quantum annealer itself: the set of spins, their local fields h_i , the sparse coupling graph defined by J_{ij} , and the current point on the schedule $(s, A(s), B(s))$. By mirroring the hardware’s native graph and control parameters in the model’s input, we ensure the learned digital twin is naturally aligned to the problem structure and the time-dependent evolution.

The model uses one token for each qubit i with computational basis value $x_i \in \{-1, +1\}$. Each token carries static node features such as the local field h_i , the degree $d_i = \sum_j \mathbf{1}_{J_{ij} \neq 0}$, and the weighted degree $w_i = \sum_j |J_{ij}|$. Global context comprises the parameter s and the instantaneous coefficients $A(s)$ and $B(s)$. We inject s by means of a global context token $[\text{CLS}]_s$ that participates in attention – following the common use of a class token for sequence-level aggregation in Transformer models [27, 28], and by FiLM-style affine conditioning that modulates intermediate activations [29]. To encode topology we supply graph positional channels built from Laplacian eigenvectors $\{\phi_k(i)\}$ and random-walk features, which are learned jointly so that locality induced by the couplings $\{J_{ij}\}$ is preserved [30, 31].

Self attention is masked to the coupling graph so that tokens attend only to neighbors with $|J_{ij}| > 0$. When larger receptive fields are beneficial we expand this mask to k hop neighborhoods. This masking yields per layer complexity that scales with $|E|$ on sparse graphs rather than with N^2 . For dense instances such as our RHM suite (complete interaction graph, $|E| = \Theta(N^2)$), this masking becomes effectively dense and the attention term reverts to $\Theta(N^2)$ scaling. The $|E|$ -based expression remains valid but no longer yields sparsity savings. The backbone consists of L transformer blocks with pre LN normalization, residual connections, and gated feed forward layers. We use rotary position mixing for stability across varying N . The global context token aggregates system level statistics and provides a route for long range information flow without creating dense attention among all pairs of nodes.

On top of this backbone we place lightweight heads that produce a variational wavefunction $\Psi_\theta(x; s)$. Because $H_{QA}(s)$ is real in the computational basis and our experiments focus on this setting, we work in a real gauge throughout and parameterize all modeled eigenstates with real amplitudes. Concretely, for the ground state we often enforce nonnegativity via $\Psi_{0,\theta}(x; s) = \exp\{g_{0,\theta}(x; s)\}$ because it improves the numerical stability of Monte-Carlo estimators, while for excited states

we use a separate head with an unconstrained real output $\Psi_{k,\theta}(x; s) = \tilde{g}_{k,\theta}(x; s)$ to allow sign changes. In this real gauge the FOAPT transition matrix element $M_{01}(s) = \langle \Psi_0(s) | \frac{dH_{QA}}{ds} | \Psi_1(s) \rangle$ is also real and can be estimated using the same samples. Expectations are taken with respect to $|\Psi_\theta(x; s)|^2$. We use Metropolis–Hastings sampling with proposals whose acceptance ratio

$$a(x \rightarrow x') = \min \left\{ 1, \frac{|\Psi_\theta(x'; s)|^2}{|\Psi_\theta(x; s)|^2} \right\} \quad (7)$$

is cheap to evaluate because all configurations in the mini-batch share the same masked graph and schedule context, so the transformer can be reused efficiently.

Training at a fixed s proceeds until the energy estimate stabilizes under a variance-based test that is robust to sampling noise. Concretely, we monitor the standard deviation of the energy over the most recent n epochs and stop when it drops below a target ϵ_{var} ; as secondary checks we require an effective sample size above a user-set ESSmin and gradient norms below a cap gradmax. This policy keeps wall-time roughly uniform across s , automatically spends more effort near small gaps (where variance decays slowly), and produces wavefunctions accurate enough to feed the FOAPT-style control functional in Sec. 2.4. Because attention is graph-masked and parameters are shared across s through the global context token, we can also refine the grid in s to be denser near predicted gap regions, which is essential for instance-specific schedule synthesis.

2.3. Excited-State Modeling with Brauer Deflation and Transfer Learning

Thus far we have described how the Tx-NQDT learns the ground state of $H_{QA}(s)$ across the anneal. We now extend the framework to also model low-lying excited states, which is crucial for predicting the minimum gap $\Delta(s)$ and the nonadiabatic couplings. A direct approach to train excited-state neural wavefunctions would be to enforce orthogonality to the ground state (e.g. via Gram–Schmidt or penalty terms) while variationally minimizing the excited-state energy. However, such techniques can be numerically unstable in high-dimensional spaces and difficult to scale. Instead, we adopt a deflation strategy based on Brauer’s theorem that allows us to recycle the learned ground state and efficiently train a model for the first excited state without explicit orthogonalization. The key idea is to use a rank-one perturbation to lift the energy of an already-known eigenstate, so that the next eigenstate becomes the ground state of a slightly modified Hamiltonian. Because our neural ansatz shares parameters across different states and values of s , we can reuse most of the learned features and only make minimal adjustments to capture the excited state, significantly reducing the additional cost of excited-state training.

Brauer’s theorem (1952 [32]) formalizes how a rank-one update to a Hermitian matrix affects its spectrum. In

essence, adding a projector onto an eigenvector raises (or lowers) that eigenvalue while leaving all other eigenpairs unchanged.

Let $H \in \mathbb{C}^{n \times n}$ be Hermitian with eigenpairs $(\lambda_i, \mathbf{u}_i)_{i=1}^n$ and let \mathbf{u}_k be the eigenvector we already know. For any vector \mathbf{v} , the perturbed matrix

$$\tilde{H} = H + \mathbf{u}_k \mathbf{v}^\dagger \quad (8)$$

has the same eigenvalues as H except that λ_k is shifted to $\lambda_k + \mathbf{v}^\dagger \mathbf{u}_k$, and \mathbf{u}_k remains an eigenvector. Choosing $\mathbf{v} = \delta \mathbf{u}_k$ produces

$$\tilde{H} = H + \delta \mathbf{u}_k \mathbf{u}_k^\dagger, \quad (9)$$

which lifts only the k -th eigenvalue by δ and leaves all other eigenvalues and eigenvectors unchanged.

Theorem 1. *Let H be an $n \times n$ Hermitian matrix with eigenvalues $\lambda_1 \leq \dots \leq \lambda_n$, and let \mathbf{u}_i be the eigenvector corresponding to λ_i . For any n -dimensional vector \mathbf{v} , the matrix $\tilde{H} = H + \mathbf{u}_i \mathbf{v}^\dagger$ has eigenvalues $\lambda_1, \dots, \lambda_i + \mathbf{v}^\dagger \mathbf{u}_i, \dots, \lambda_n$. Moreover, \mathbf{u}_i remains an eigenvector of \tilde{H} with eigenvalue $\lambda_i + \mathbf{v}^\dagger \mathbf{u}_i$.*

Proof. See Appendix B.

A direct corollary of the theorem shows that choosing $\mathbf{v} = \delta \cdot \mathbf{u}_i$ shifts only the eigenvalue associated with \mathbf{u}_i , leaving all other eigenpairs unchanged.

Corollary 1. *Let H be an $n \times n$ Hermitian matrix with eigenvalues $\lambda_1 \leq \dots \leq \lambda_n$, and \mathbf{u}_i be the **normalized** eigenvector corresponding to λ_i . Then the matrix $\tilde{H} = H + \delta \cdot \mathbf{u}_i \mathbf{u}_i^\dagger$ has eigenvalues $\lambda_1, \dots, \lambda_i + \delta, \dots, \lambda_n$ and the same eigenvectors as H .*

Proof. See Appendix B.

We apply this construction to the annealing Hamiltonian. After we have trained the transformer to approximate the ground state of $H_{QA}(s)$, we form the deflated Hamiltonian

$$H_{QA}^{(1)}(s) = H_{QA}(s) + \delta_0 \frac{|\Psi_0(s)\rangle\langle\Psi_0(s)|}{\langle\Psi_0(s)|\Psi_0(s)\rangle}, \quad (10)$$

where $\delta_0 \in \mathbb{R}$ is chosen on the order of $|E_0(s)|$ so that the learned ground state is pushed above the first true excited state. Under this perturbation, the physical first excited state of $H_{QA}(s)$ becomes the ground state of $H_{QA}^{(1)}(s)$, and we can train exactly as before but now targeting that new ground state. All other eigenstates keep their eigenvectors, so the procedure is spectrally well behaved.

Architecturally, we keep a single shared transformer backbone \mathcal{T}_ϕ that encodes $(x, h, J, s, A(s), B(s))$ with the graph-masked attention, and we attach separate, lightweight output heads for each state:

$$\Psi_k(x; s) = \mathcal{H}_k(\mathcal{T}_\phi(x, h, J, s)), \quad k = 0, 1, \dots \quad (11)$$

State $k = 0$ is trained on $H_{\text{QA}}(s)$; state $k = 1$ is trained on $H_{\text{QA}}^{(1)}(s)$ using the same sampling, variance-based stopping, and optimizer. Higher states can be obtained by iterating the same rank-one deflation. Because the backbone parameters ϕ already encode the problem graph and the instantaneous anneal coefficients, we can either freeze ϕ and train only \mathcal{H}_1 (cheapest), or fine-tune ϕ with a reduced learning rate to let the representation adjust to the deflated Hamiltonian. In practice this gives a clear wall-time reduction compared to retraining a separate network from scratch for every state.

To guard against imperfect deflation and sampling noise, we optionally add a small orthogonality penalty

$$\mathcal{L}_\perp = \lambda_\perp \left| \langle \Psi_0(s) | \Psi_1(s) \rangle \right|^2, \quad (12)$$

where the overlap is estimated from the same Monte-Carlo samples used for the energy. This keeps the learned Ψ_1 from drifting back toward Ψ_0 when the gap is very small or when δ_0 is chosen conservatively.

Finally, we propagate these models along the annealing parameter by transfer learning. After training at $s = a$, we initialize the model for $s = a + \Delta s$ with the parameters learned at $s = a$ (both backbone and the relevant heads). Because adiabatic spectra evolve smoothly in s , this warm start greatly shortens convergence, maintains temporal coherence of both $E_0(s)$ and $E_1(s)$, and lets us refine the s -grid near predicted gap locations without multiplying the total cost. The result is a scalable procedure that (i) extracts the low-energy spectrum needed by the FOAPT-style control in Sec. 2.4, (ii) avoids explicit Gram–Schmidt or projection methods that are numerically brittle in high dimension, and (iii) stays compatible with hardware-style $A(s), B(s)$ schedules.

On top of the shared backbone we attach two heads, one dedicated to the ground state and one dedicated to the first excited state. Throughout this paper we work in a real gauge, hence each head outputs a real scalar $\Psi_k(x; s)$ that represents the wavefunction amplitude of the input configuration at anneal parameter s . For the ground state we may enforce nonnegativity by writing $\Psi_0(x; s) = \exp\{g_\theta(x; s)\}$ for numerical stability, and for the first excited state we allow sign changes and take $\Psi_1(x; s) = \tilde{g}_\theta(x; s)$ as an unconstrained real output. Given a specific spin configuration as input, the scalar produced by the corresponding head is interpreted as the real amplitude of that configuration. Probabilities follow the Born rule after normalization,

$$p_k(x; s) = \frac{\Psi_k(x; s)^2}{Z_k(s)}, \quad Z_k(s) = \sum_{x'} \Psi_k(x'; s)^2, \quad (13)$$

with $Z_k(s)$ computed implicitly by sample-based estimators or exactly by enumeration for small systems as detailed in Section 2.2 and Section 3.3.

This shared backbone with per-state heads reuses features across states and along the anneal parameter, supports stable reconstruction of low-lying spectra needed

for schedule synthesis, and prepares the ground for the deflation-based procedure developed later in this section.

The proposed Tx-NQDT framework extends naturally to higher excited states by iteratively applying Brauer-based perturbations. Each excited state is obtained as the ground state of a modified Hamiltonian. The method does not require changes to the network architecture, optimization strategy, or stopping criterion, making it robust and scalable for resolving the low-energy spectrum. This eliminates the need for explicit orthogonalization methods, such as Gram–Schmidt or projection-based deflation, which can suffer from numerical instability and orthogonality loss in high-dimensional spaces.

2.4. Instantaneous Energy Gap and Nonlinear Annealing Schedules

A key advantage of the Tx-NQDT is that it provides direct access to spectral quantities that real hardware cannot directly measure, namely the instantaneous energy gap $\Delta(s)$ and the matrix elements governing nonadiabatic transitions. With these quantities in hand, we can design instance-specific annealing schedules that slow down exactly where the problem instance requires more time (near small gaps) and speed up where the gap is large, thereby improving the probability of remaining in the ground state. In this subsection, we describe how the Tx-NQDT outputs are used to construct such adaptive schedules based on first-order adiabatic perturbation theory (FOAPT).

Once the Tx-NQDT has been trained over the interval $s \in [0, 1]$, we obtain, for each value of s , approximations of the ground state $|\Psi_0(s)\rangle$ and first excited state $|\Psi_1(s)\rangle$, together with their corresponding energies $E_0(s)$ and $E_1(s)$. From these quantities, we compute the instantaneous spectral gap

$$\Delta(s) = E_1(s) - E_0(s), \quad (14)$$

and the nonadiabatic coupling between these two states given by the off-diagonal matrix element

$$M_{01}(s) = \langle \Psi_0(s) | \frac{dH_{\text{QA}}}{ds} | \Psi_1(s) \rangle. \quad (15)$$

We estimate $M_{01}(s)$ using Monte Carlo sampling by drawing configurations x from the probability distribution $|\Psi_0(s)|^2$ and evaluating $\frac{dH_{\text{QA}}}{ds}$ —which is known analytically from the Hamiltonian—on these samples to compute the expectation value. Intuitively, the gap $\Delta(s)$ identifies where along the anneal path the system is most vulnerable (small $\Delta(s)$ indicates an avoided crossing or phase transition), while $M_{01}(s)$ quantifies how strongly the time-dependent driving term induces transitions at that point. Together, these functions determine the adiabatic hardness of different regions of the anneal.

According to adiabatic perturbation theory, a sufficient condition for the evolution to remain approximately in

the instantaneous ground state is

$$\frac{|\langle \Psi_0(s) | \frac{dH_{QA}}{dt} | \Psi_1(s) \rangle|}{\Delta(s)^2} \ll 1, \quad (16)$$

for all physical times t during the anneal. Here t denotes physical time, and by the chain rule

$$\frac{dH_{QA}}{dt} = \frac{dH_{QA}}{ds} \frac{ds}{dt}. \quad (17)$$

Rearranging the inequality to isolate the time derivative of s , we define the *adiabatic control functional*

$$\Lambda(s) = \frac{|\langle \Psi_0(s) | \frac{dH_{QA}}{ds} | \Psi_1(s) \rangle|}{\Delta(s)^2} = \frac{|M_{01}(s)|}{\Delta(s)^2}. \quad (18)$$

The adiabatic condition then approximately requires

$$\Lambda(s) \left| \frac{ds}{dt} \right| \ll 1 \quad \text{for all } s \in [0, 1]. \quad (19)$$

In this form, $\Lambda(s)$ quantifies the local “difficulty” of the anneal: when $\Lambda(s)$ is large, the schedule should progress more slowly (small ds/dt) at that point; when $\Lambda(s)$ is small, the evolution can proceed more rapidly. This motivates choosing a rescaled annealing schedule $s(t)$ that allocates time inversely proportional to $\Lambda(s)$. Specifically, we set

$$\frac{ds}{dt} = \frac{\Lambda(s_r)}{\Lambda(s)}, \quad (20)$$

where s_r is a reference point along the anneal. In practice, we typically choose $s_r = 0$, the start of the anneal, where $\Lambda(0)$ is often relatively small because the spectral gap is large and the system begins in a simple product state. This choice also ensures that

$$\left. \frac{ds}{dt} \right|_{s=0} = 1 \quad (21)$$

in normalized units, so that the anneal starts at full speed.

The differential equation above implies that

$$\Lambda(s) \frac{ds}{dt} = \Lambda(s_r) \quad (22)$$

is held constant along the anneal path. Integrating, we obtain the cumulative time required to reach a point s :

$$t(s) = \int_{s_r}^s \frac{\Lambda(u)}{\Lambda(s_r)} du, \quad (23)$$

up to an overall scaling by the total anneal duration T if physical units are desired. This first-order optimal annealing law stretches the schedule in regions of large $\Lambda(s)$ (corresponding to narrow gaps or strong nonadiabatic couplings) and compresses it in regions of small $\Lambda(s)$, ideally keeping the adiabatic gauge $\Lambda(s) ds/dt$ approximately constant throughout the evolution. This

construction is rooted in first-order adiabatic perturbation theory (FOAPT) and closely related local-adiabatic strategies studied in the literature.

In practice, additional constraints must be incorporated to make the schedule implementable on real hardware. Most quantum annealers, including D-Wave systems, allow only a limited number of piecewise-linear segments and impose a maximum admissible slope for $s(t)$ due to control hardware limitations. In our implementation, we address these constraints as follows (More details are in Appendix C):

1. Piecewise-linear equal-mass discretization:

We first build a piecewise-linear $s(t)$ whose breakpoints are chosen so that each segment integrates the same “mass” $\Lambda(s) ds$. This concentrates knots in regions where Tx-NQDT predicts narrow gaps or strong transition matrix elements, and keeps the number of pieces modest (e.g., $K = 12$).

2. Global slope cap:

Real devices impose a maximal admissible ramp rate. We therefore enforce a hard constraint $\frac{ds}{dt} \leq 2.0 (\mu s)^{-1}$ on every segment when we time-parameterize the knots. This guarantees that the synthesized schedule remains compatible with hardware limits while still reflecting the FOAPT-derived density $\Lambda(s)$.

Figure 1 summarizes the full Tx-NQDT workflow. Panel (a) shows the end-to-end pipeline. A problem instance, specified by local fields and couplings (h, J) together with hardware constraints (maximum slope and number of control points), is first discretized along the anneal parameter $s \in [0, 1]$. At each discretized point, the Tx-NQDT produces variational estimates of the ground-state energy $E_0(s)$, first-excited-state energy $E_1(s)$, the instantaneous gap $\Delta(s)$, and the transition matrix element $\langle \Psi_0(s) | dH_{QA}/ds | \Psi_1(s) \rangle$. These quantities are used to construct a first-order adiabatic perturbation theory (FOAPT) control functional, from which an adaptive, piecewise-linear annealing schedule is synthesized subject to hardware constraints. Panel (b) illustrates the internal structure of the Tx-NQDT. A graph-aware Transformer with masked self-attention aligned to the Ising coupling graph takes as input a spin configuration, the problem graph, and the current anneal parameter. A shared backbone encodes instance-level structure, while lightweight output heads represent the wavefunction amplitudes of the ground and excited states. The learned states are used both for spectral reconstruction and for evaluating the control functional driving schedule optimization. Together, this pipeline forms a closed-loop workflow from data-driven spectral reconstruction to hardware-compatible annealing control, making excited-state information operationally useful for near-term quantum annealers.

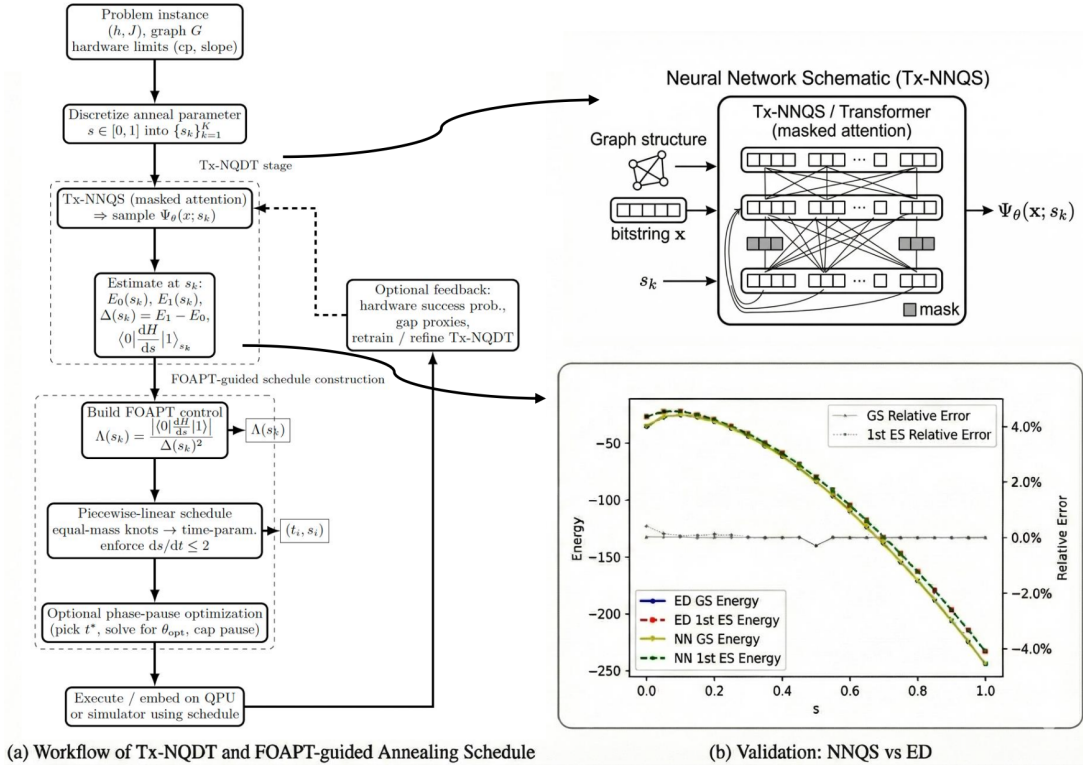


FIG. 1: Tx-NQDT pipeline with FOAPT-guided schedule construction.

3. SIMULATION EXPERIMENTS

We conduct numerical simulation experiments to evaluate the accuracy, robustness, and scalability of the proposed Tx-NQDT framework for simulating quantum annealing under time-dependent Hamiltonians. The experiments are designed with three complementary goals: (i) to validate spectral accuracy against exact numerical references where feasible, (ii) to assess generalization beyond structured benchmark models, and (iii) to demonstrate scalability to system sizes where exact simulation becomes impractical.

We consider two representative model families throughout: (i) **the Transverse-Field Ising Model (TFIM)**, which provides a clean, structured benchmark with well-understood spectral properties, and (ii) **Random Hamiltonian Models (RHM)**, which serve as proxies for generic, non-integrable many-body systems encountered in realistic annealing workloads.

We study system sizes $N = 6, 10, 15$, and 20 . The smallest case, $N = 6$, is used purely as a *toy validation example*, where full exact diagonalization (ED) is trivial and results can be easily verified independently. The intermediate sizes $N = 10$ and $N = 15$ form the *main validation regime*: they are large enough to be nontrivial yet still admit exact numerical references along the anneal path. Finally, $N = 20$ serves as a *scalability test*: here the Hilbert space dimension (2^{20}) makes ED impractical, and we assess whether Tx-NQDT continues to

produce stable, physically consistent spectra suitable for downstream schedule design.

3.1. Benchmark: Transverse-Field Ising Model (TFIM)

We first benchmark Tx-NQDT on the transverse-field Ising model (TFIM), a standard test case for quantum annealing due to its well-characterized spectrum and the presence of near-degeneracies between the ground and first excited states as the transverse field is turned off [23, 33]. This makes TFIM an ideal setting to verify whether the proposed digital twin can correctly track level ordering, avoided crossings, and wavefunction evolution along the anneal.

We consider the canonical open-chain TFIM with no longitudinal fields, $h_i = 0$, and ferromagnetic nearest-neighbor couplings $J_{i,i+1} = 1$, with all other $J_{ij} = 0$. This model captures the essential ingredients of quantum annealing—competition between transverse-field delocalization and Ising interactions—without introducing disorder that could obscure modeling errors.

We do not perform TFIM experiments at $N = 10, 15$, or 20 . For larger system sizes, we focus exclusively on random Hamiltonian models (RHM), which provide a more representative and challenging test of the digital twin in dense, non-integrable many-body settings relevant for schedule design.

3.2. Generalization: Random Hamiltonian Models (RHM)

To assess generalization beyond structured models, we apply Tx-NQDT to random Hamiltonian models (RHM), which provide a significantly more challenging test due to dense interactions and highly instance-dependent spectral structure.

For each system size $N \in \{10, 15, 20\}$, we generate a total of 20 random instances, which are subsequently classified into easy and hard cases based on their minimum spectral gaps. Each instance corresponds to one many-body Hamiltonian defined by a specific pair (h, J) , where all local fields h_i and couplings J_{ij} ($i < j$) are drawn independently from a uniform distribution on $[-5, 5]$. Because all couplings are almost surely nonzero, the interaction graph is complete, with $|E| = N(N-1)/2 = \Theta(N^2)$.

For $N = 10$ and $N = 15$, exact diagonalization is still feasible and provides reference spectra along the anneal. These sizes are therefore used to quantify the accuracy of Tx-NQDT in terms of eigenvalues and wavefunctions, and to verify that the learned spectral information correctly identifies regions requiring schedule slow-down. For $N = 20$, ED is no longer practical. In this regime, we use the same instance-generation protocol and training pipeline, but rely exclusively on Tx-NQDT predictions. This mirrors the realistic setting in which digital twins are intended to operate.

Easy versus hard instances. Random instances are classified as *easy* or *hard* according to their minimum spectral gap

$$\Delta_{\min} = \min_{s \in [0,1]} (E_1(s) - E_0(s)). \quad (24)$$

Instances with relatively large Δ_{\min} are labeled easy, as adiabatic tracking is less demanding and nonadiabatic transitions are suppressed. Instances with small Δ_{\min} are labeled hard and exhibit narrow avoided crossings and stronger eigenstate mixing. This classification provides a controlled way to evaluate Tx-NQDT under both favorable and adversarial spectral conditions.

3.3. Training Protocol and Implementation Details

Across all experiments, we discretize the anneal parameter $s \in [0, 1]$ into 21 equally spaced points with step size $\Delta s = 0.05$. This grid is fine enough to resolve narrow gaps while keeping the overall computational cost manageable, and is held fixed across all system sizes for consistency.

At each s , we train Tx-NQDT to approximate the in-

stantaneous ground and first excited states of

$$H_{QA}(s) = -\frac{A(s)}{2} \sum_i \hat{\sigma}_x^i + \frac{B(s)}{2} \left(\sum_i h_i \hat{\sigma}_z^i + \sum_{i>j} J_{ij} \hat{\sigma}_z^i \hat{\sigma}_z^j \right), \quad (25)$$

using the masked Transformer architecture described in Sec. 2.

For each value of s , we train first on the ground state using variational Monte Carlo (VMC). Samples $x \sim |\Psi_\theta(x; s)|^2$ are drawn using Metropolis–Hastings with single-spin flip proposals. When the autoregressive auxiliary head is enabled, we occasionally replace a Markov proposal by an independent draw from the factorized head. This reduces autocorrelation and is particularly helpful near small gaps, where VMC estimators can become noisy.

On each accepted configuration we evaluate the local energy

$$E_{\text{loc}}(x; \theta, s) = \frac{\langle x | H_{QA}(s) | \Psi_\theta(\cdot; s) \rangle}{\Psi_\theta(x; s)}, \quad (26)$$

and form the standard VMC gradient estimate

$$\nabla_\theta \mathcal{L}(s) \approx 2 \mathbb{E}_{x \sim |\Psi_\theta|^2} [(E_{\text{loc}}(x; \theta, s) - \bar{E}(s)) \times \nabla_\theta \log |\Psi_\theta(x; s)|], \quad (27)$$

where $\bar{E}(s)$ denotes the running energy mean. The transformer thus plays the role of the variational ansatz, while the optimization loop follows the standard stochastic re-configuration / VMC paradigm.

Optimization uses AdamW with learning rate 3×10^{-4} , cosine decay after a short warm-up, weight decay 10^{-4} , and gradient clipping at norm 1. We monitor three stability signals at each s : the standard deviation of recent energy estimates, the effective sample size of the Markov chain, and the gradient norm. Training at that s stops as soon as the variance falls below a tolerance ε_{var} and the other two signals are in range. To avoid runaway runtimes, we also cap the number of optimization steps per s to a fixed budget, ensuring predictable wall-clock cost even for $N = 20$.

For $N = 10$ and $N = 15$ we verify the learned spectra by explicit diagonalization of the $2^N \times 2^N$ Hamiltonian built from the same $(A(s), B(s), h, J)$, and we report errors for both $E_0(s)$ and $E_1(s)$. For $N = 20$, the identical training and diagnostic pipeline is used, but without ED reference; these runs are used to assess stability and scalability rather than absolute accuracy.

3.4. Spectral Accuracy and Scaling Results

Figure 2 shows the hardware-style annealing coefficients $A(s)$ and $B(s)$ used throughout all experiments.

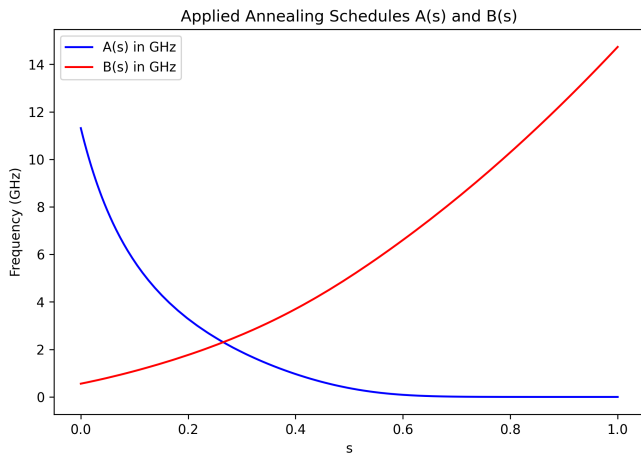


FIG. 2: D-Wave hardware annealing coefficients $A(s)$ (driver) and $B(s)$ (problem) as functions of the normalized anneal parameter s . These curves are the schedule inputs used in our Tx-NQDT experiments.

These curves define the baseline schedule whose spectral properties Tx-NQDT is trained to reproduce and later exploit for schedule optimization.

Figure 3 compares exact and learned spectra for representative easy and hard instances at $N = 6, 10, 15$, and shows learned spectra at $N = 20$. At $N = 6$, the learned spectra are obtained with the MLP baseline model (Appendix G), whereas for $N \geq 10$ they are produced by the Transformer-based Tx-NQDT. Across all verified cases ($N = 6, 10, 15$), the learned spectra closely track both ground and first excited energies along the full anneal. Deviations are localized near narrow-gap regions where eigenstate mixing is strongest and variational Monte Carlo estimators are most challenging. At $N = 20$, although no exact reference is available, the learned spectra remain smooth, well ordered, and consistent with trends observed at smaller system sizes.

Table I summarizes the relative errors of Tx-NQDT-predicted ground- and first-excited-state energies across representative anneal points and system sizes, from which three consistent patterns emerge. First, relative errors are typically largest near the beginning of the anneal ($s \lesssim 0.1$), particularly for excited states and for larger N , reflecting higher estimator variance in the driver-dominated regime. Second, errors decrease rapidly as s increases and remain small throughout the mid-to-late anneal region ($s \gtrsim 0.4$), which is the regime most relevant for adiabatic dynamics and schedule optimization. Third, across all cases the mean error over the full anneal remains modest, with maxima localized to early- s points and minima generally attained near the end of the anneal. Importantly, this qualitative behavior is consistent across TFIM, easy RHM, and hard RHM instances.

Crucially, the elevated errors near $s \approx 0$ do not compromise the usefulness of Tx-NQDT for dynamics prediction or schedule design. In the driver-dominated regime

the instantaneous gap $\Delta(s)$ is typically large, strongly suppressing nonadiabatic transitions. Both adiabatic and FOAPT-based error estimates weight contributions by inverse powers of $\Delta(s)$, so inaccuracies in this region contribute negligibly to excitation probability and therefore receive little time allocation in optimized schedules. By contrast, the narrow-gap regions later in the anneal—where schedule adaptation matters most—are precisely where Tx-NQDT achieves its highest spectral fidelity.

Runtime scaling is summarized in Fig. 4, which reports the end-to-end epoch time for Transformer-NNQS ground-state training at a fixed anneal point ($s = 0$). Each data point shows the mean epoch time averaged over epochs 6–25 (to exclude warm-up effects), with error bars indicating the minimum and maximum epoch times over the same window, thereby capturing within-run variability due to sampling noise and system scheduling. All measurements were performed on an Apple M2 chip using one representative dense RHM instance per system size. The measured mean epoch times increase smoothly with system size, from approximately 2.1 s at $N = 6$ to 8.6 s at $N = 20$, and are well fitted by a quadratic-linear model $t_{\text{epoch}}(N) = t_0 + aN + bN^2$ with $R^2 = 0.996$. For dense RHM instances, the dominant per-epoch costs arise from masked self-attention and energy/observable evaluation, both of which scale as $\mathcal{O}(N^2)$ due to the fully connected coupling graph. In the small- N regime considered here ($N \leq 20$), constant overheads—such as kernel dispatch, framework bookkeeping, and sampling management—partially mask the asymptotic behavior, making the observed growth appear closer to linear; nevertheless, the fitted model confirms predictable scaling consistent with the architecture. Consistent with this cost profile, convergence traces show that training typically stabilizes within ~ 20 epochs at $s = 0.1$ for $N = 10, 15, 20$, and within ~ 10 epochs at $s = 0.8$, demonstrating stable and rapid convergence for both ground and excited states across all system sizes.

Taken together, these results show that Tx-NQDT delivers high-fidelity spectral reconstructions where exact verification is possible ($N \leq 15$), degrades gracefully near small gaps, and scales reliably to larger systems ($N = 20$), where it provides precisely the spectral information required for adaptive annealing schedule design.

4. D-WAVE OPTIMIZATION EXPERIMENTS

A key objective of the Tx-NQDT framework is to translate learned spectral information into *hardware-executable* annealing schedules that improve performance on real quantum annealers. In this section, we empirically validate this simulation-to-hardware pipeline on a D-Wave Advantage system, quantifying the impact of Tx-NQDT-optimized schedules on ground-state recovery for quadratic unconstrained binary optimization (QUBO) problems.

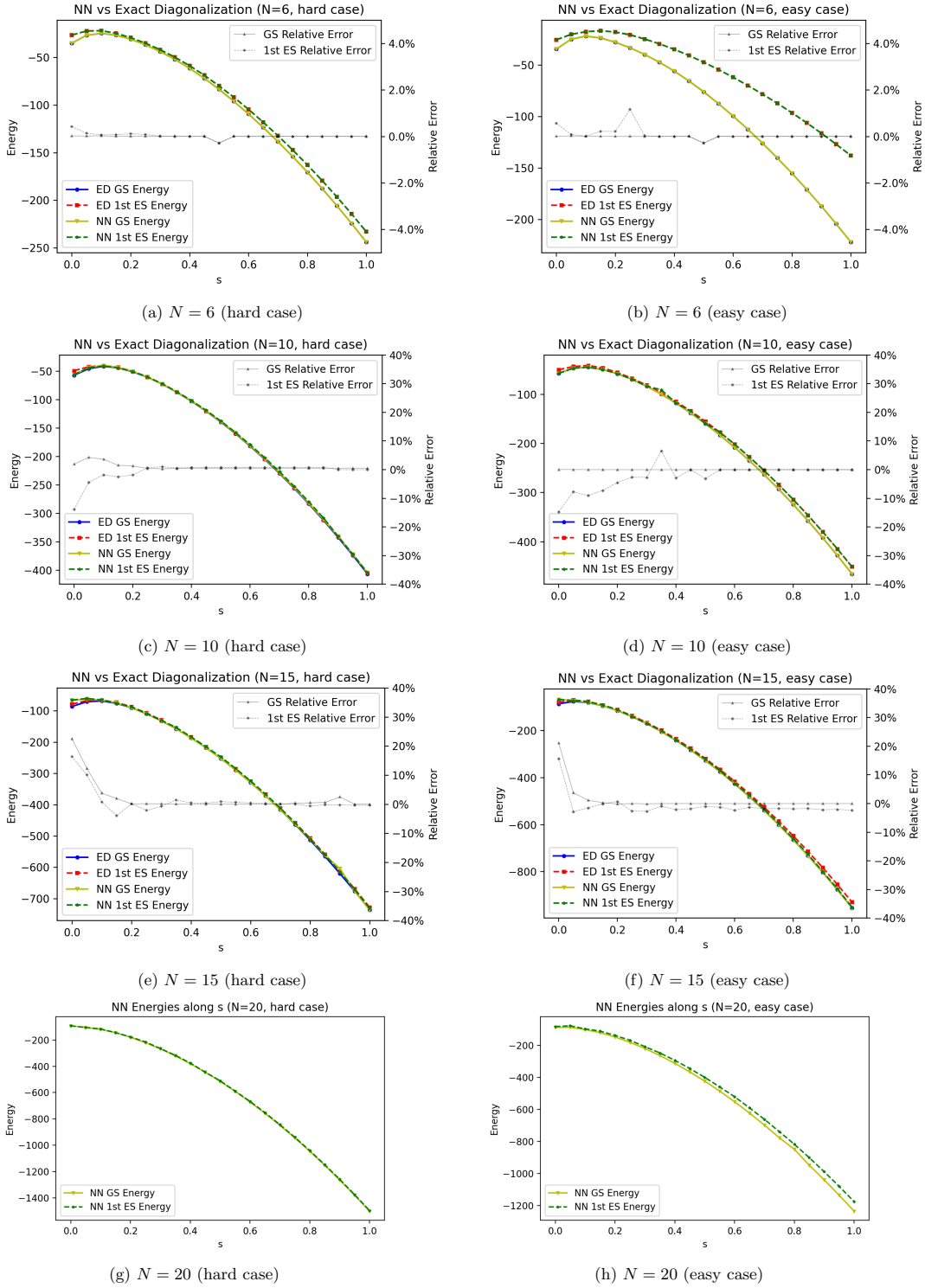


FIG. 3: Exact vs. learned spectra for representative easy and hard instances at system sizes $N = 6, 10, 15$, and learned spectra at $N = 20$.

a. Problem instances and hardware embedding. We benchmark on randomly generated QUBO instances with logical problem sizes $N = 10, 15$, and 20 . For each system size, we evaluate 20 independent instances, yielding

a total of 60 problems. Each instance corresponds to a distinct pair of local fields and couplings (h, J) , drawn uniformly from $[-5, 5]$, and is mapped to an equivalent Ising Hamiltonian via the standard QUBO–Ising trans-

N	case	level	Early s		Mid s		Late s		All s stats		
			0.00	0.20	0.40	0.60	0.80	1.00	Mean	Max	Min
6	TFIM	GS	0.000	0.000	0.000	0.000	0.000	0.000	2.5×10^{-4}	0.001	0.000
6	TFIM	ES	0.002	0.001	0.000	0.000	0.000	0.000	4.4×10^{-4}	0.002	0.000
6	easy	GS	0.000	0.000	0.000	0.000	0.000	0.000	-1.4×10^{-4}	0.000	-0.003
6	easy	ES	0.006	0.002	0.000	0.000	0.000	0.000	2.1×10^{-4}	0.012	-0.003
6	hard	GS	0.000	0.000	0.000	0.000	0.000	0.000	-1.4×10^{-4}	0.000	-0.003
6	hard	ES	0.004	0.001	0.000	0.000	0.000	0.000	1.1×10^{-4}	0.004	-0.003
10	easy	GS	0.000	0.000	0.000	0.000	0.000	0.000	4.8×10^{-5}	0.001	0.000
10	easy	ES	-0.147	-0.045	-0.029	0.000	0.000	0.000	-3.7×10^{-2}	0.065	-0.147
10	hard	GS	0.019	0.013	0.005	0.005	0.005	0.005	1.1×10^{-2}	0.043	0.003
10	hard	ES	-0.138	-0.018	0.008	0.008	0.008	0.000	-1.5×10^{-2}	0.010	-0.138
15	easy	GS	0.212	-0.001	0.000	0.000	0.000	0.000	1.3×10^{-2}	0.212	-0.001
15	easy	ES	0.157	0.007	-0.021	-0.023	-0.018	-0.023	-1.4×10^{-2}	0.157	-0.027
15	hard	GS	0.225	0.001	0.000	0.000	0.005	0.000	1.8×10^{-2}	0.225	0.000
15	hard	ES	0.163	0.001	0.005	0.004	-0.006	-0.004	9.6×10^{-3}	0.163	-0.040

TABLE I: Signed relative error of model-predicted energies versus exact diagonalization. Results are computed on a grid of 21 anneal points $s \in [0, 1]$; due to space constraints, only representative early, mid, and late s values are reported here. Mean, maximum, and minimum errors are computed over all 21 points. The qualitative performance is similar across the omitted intermediate points. The $N = 6$ block reports the small- N MLP baseline (Appendix G), whereas the $N \geq 10$ blocks report the Transformer-based Tx-NQDT results.

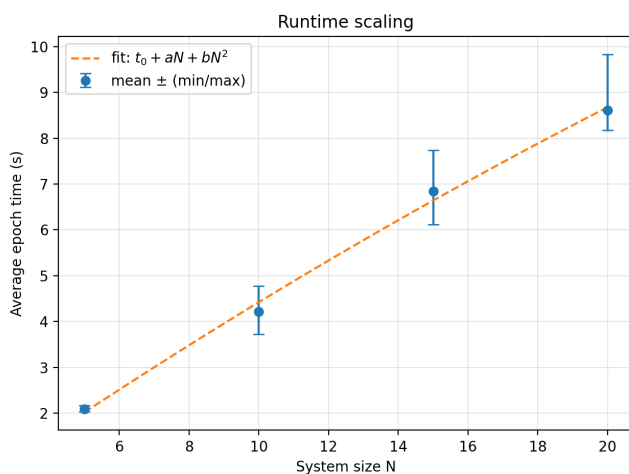


FIG. 4: Runtime scaling on Apple M2. Mean epoch wall-clock time versus system size N at fixed $s = 0$ (blue: mean over epochs 6 – 25; error bars: min/max over the same window). The dashed line is a least-squares fit $t_{\text{epoch}}(N) = t_0 + aN + bN^2$.

formation. The resulting logical problems are embedded onto the Pegasus topology of the D-Wave Advantage processor using the Ocean SDK. Logical qubits are mapped to chains of physical qubits, with chain strengths tuned to balance logical fidelity and robustness against chain breaks. All couplings are rescaled to satisfy hardware constraints.

b. Instance difficulty classification. As in the simulation study, we classify instances into *easy* and *hard* subsets based on their intrinsic adiabatic difficulty. Specifically, for each instance we estimate the minimum instantaneous spectral gap

$$\Delta_{\min} := \min_{s \in [0,1]} (E_1(s) - E_0(s))$$

from the Tx-NQDT digital twin. Instances with relatively large Δ_{\min} are labeled *easy*, while those with smaller Δ_{\min} are labeled *hard*. This criterion is physically motivated: a small minimum gap indicates a pronounced bottleneck for adiabatic evolution and is generally associated with increased susceptibility to nonadiabatic transitions, making schedule design and high-fidelity execution more challenging. For each N , we evaluate 10 easy and 10 hard instances.

c. Construction of hardware-compatible schedules. Using the Tx-NQDT estimates of the instantaneous gap and transition matrix elements, we construct adaptive annealing schedules following first-order adiabatic perturbation theory (FOAPT). With reference point $s_r = 0$, the adiabatic rescaling condition reads

$$\frac{ds}{dt} = \frac{\Lambda(0)}{\Lambda(s)} \cdot \frac{1}{T}, \quad \frac{dt}{ds} = \frac{\Lambda(s)}{\Lambda(0)} T, \quad (28)$$

yielding the cumulative physical time

$$t(s) = T \int_0^s \frac{\Lambda(u)}{\Lambda(0)} du. \quad (29)$$

We discretize $s \in [0, 1]$, evaluate $\Lambda(s_i)$ via Tx-NQDT, and approximate the integral using the trapezoidal rule,

$$\Delta t_i \approx \frac{\Lambda(s_i) + \Lambda(s_{i+1})}{2\Lambda(0)} \Delta s, \quad (30)$$

to obtain a discrete map $(t(s_i), s_i)$. Linear interpolation of the inverse map produces the annealing schedule $s(t)$.

Two hardware constraints are enforced throughout: (i) at most 12 programmable control points and (ii) a maximum slope $|ds/dt| \leq 2$. Accordingly, we subsample the continuous schedule at 12 equally spaced times and rescale any segment violating the slope bound. These constraints match those used in the FOAPT runner during simulation, ensuring consistency between digital-twin optimization and hardware execution.

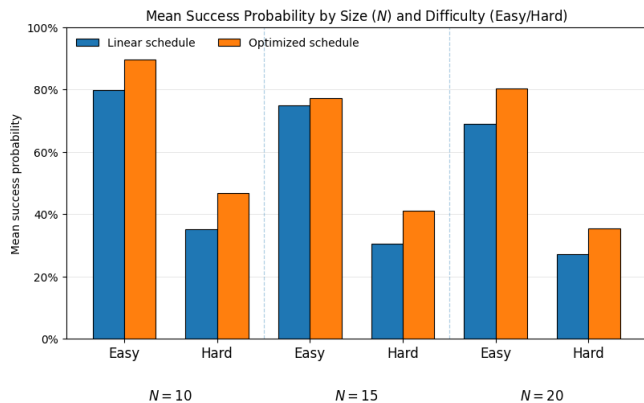


FIG. 5: Mean success probability for linear versus optimized schedules across sizes ($N = 10, 15, 20$) and difficulty subsets (easy/hard).

d. Baselines and experimental protocol. For each instance, we compare the Tx-NQDT-optimized schedule against the D-Wave default linear schedule with total duration $20 \mu\text{s}$. We deliberately do not retune the linear baseline to match the instance-dependent optimized duration T . On open-system quantum annealers, success probability is not monotonic in anneal time: longer anneals may increase thermal excitations or decoherence, while coherent diabatic effects can induce oscillatory behavior as a function of total time. Matching total duration would therefore introduce an additional tuning degree of freedom and confound schedule-shape effects. Fixing the baseline at the hardware default avoids this ambiguity and follows established benchmarking practice.

Each schedule (linear and optimized) is executed with 1000 anneals per instance. The ground-state success probability p is estimated as the empirical frequency of minimum-energy bitstrings. Each hardware experiment is repeated 10 times to reduce statistical fluctuations.

e. Empirical performance gains. Figure 5 summarizes the mean success probabilities for linear and optimized schedules across system sizes and difficulty classes. Across all three sizes, Tx-NQDT-optimized schedules outperform the linear baseline on average, with the largest relative gains observed for hard instances. Improvements persist as N increases, although their magnitude decreases, consistent with longer embedding chains and increased sensitivity to hardware noise at larger problem sizes.

Table II reports detailed statistics, including win counts and mean/median improvements. Overall, optimized schedules improve 16/20 instances at $N = 10$ (80%), 15/20 at $N = 15$ (75%), and 13/20 at $N = 20$ (65%). Gains are particularly pronounced for hard instances, where baseline success probabilities are lowest and schedule shaping has the greatest opportunity to suppress nonadiabatic transitions. Even for easy instances with already high baseline performance, optimized sched-

ules frequently yield measurable improvements.

f. Structure of optimized schedules. Representative optimized schedules are shown in Fig. 6 for easy and hard instances at $N = 10, 15$, and 20 . Across sizes and difficulty classes, the optimized schedules exhibit a characteristic slow-fast profile: an initial ramp, followed by a pronounced slowdown near the inferred small-gap region, and a subsequent acceleration once the gap reopens. This structure closely mirrors the FOAPT control functional and confirms that the digital twin correctly identifies and targets the dominant nonadiabatic bottlenecks.

Despite being optimized independently for different instances and system sizes, the schedules share a common qualitative shape. This recurrence suggests that instance-specific spectral information may be compressible into low-dimensional schedule templates, opening the possibility of fast, parametric schedule prediction without per-instance optimization.

g. Discussion. Taken together, these experiments demonstrate that Tx-NQDT can convert learned spectral information into hardware-compatible control that yields systematic and statistically significant improvements on a state-of-the-art quantum annealer. The benefits are strongest for spectrally hard instances and remain visible up to $N = 20$, despite increasing hardware noise and embedding complexity. Importantly, all improvements are achieved within the native control-point and slope limits of the device, validating Tx-NQDT as a practical digital-twin approach for spectrum-aware quantum annealing.

5. DISCUSSIONS AND CONCLUSIONS

This work establishes Transformer-based Neural Quantum Digital Twins (Tx-NQDTs) as a practical and accurate tool for reconstructing low-lying spectral properties of time-dependent many-body Hamiltonians and for translating that information into deployable quantum-annealing control. Across both structured (TFIM) and disordered (RHM) benchmarks, Tx-NQDT reliably reproduces ground- and first-excited-state energies along the full annealing path $s \in [0, 1]$. Whenever exact diagonalization (ED) is computationally feasible (here up to $N = 10, 15$), the learned spectra closely match the exact results. Although ED becomes prohibitive at $N = 20$, the same trained model continues to produce smooth and physically consistent spectral curves, indicating that the masked-attention transformer architecture is expressive enough to capture the correlations induced by strong Ising couplings under a time-dependent transverse field. This spectral fidelity is the essential prerequisite for using Tx-NQDT outputs as inputs to adiabatic-perturbation-based control.

A key practical ingredient enabling this performance is transfer along the anneal. Warm-starting the variational parameters at s_k from those converged at s_{k-1} substantially improves both numerical stability and computa-

N	subset	wins (opt>lin)	mean p_{lin}	median p_{lin}	mean p_{opt}	median p_{opt}	mean Δp	median Δp
10	easy	8/10	79.9%	84.6%	89.7%	91.1%	+9.8%	+6.5%
10	hard	8/10	35.1%	37.6%	46.8%	50.2%	+11.7%	+12.7%
15	easy	8/10	75.0%	72.4%	77.2%	79.1%	+2.2%	+6.8%
15	hard	7/10	30.4%	30.4%	41.2%	48.0%	+10.8%	+17.6%
20	easy	7/10	68.9%	75.0%	80.2%	76.1%	+11.3%	+1.1%
20	hard	6/10	27.1%	30.1%	35.5%	39.4%	+8.5%	+9.3%

TABLE II: Ground-state success probability p for linear and Tx-NQDT-optimized schedules on the D-Wave Advantage system, summarized over 20 instances per system size (10 easy and 10 hard). The column “wins (opt>lin)” reports the number of instances for which the optimized schedule achieves a strictly higher success probability than the linear baseline. Mean and median values are computed across instances within each subset.

$\Delta p := p_{\text{opt}} - p_{\text{lin}}$ denotes the per-instance improvement in success probability.

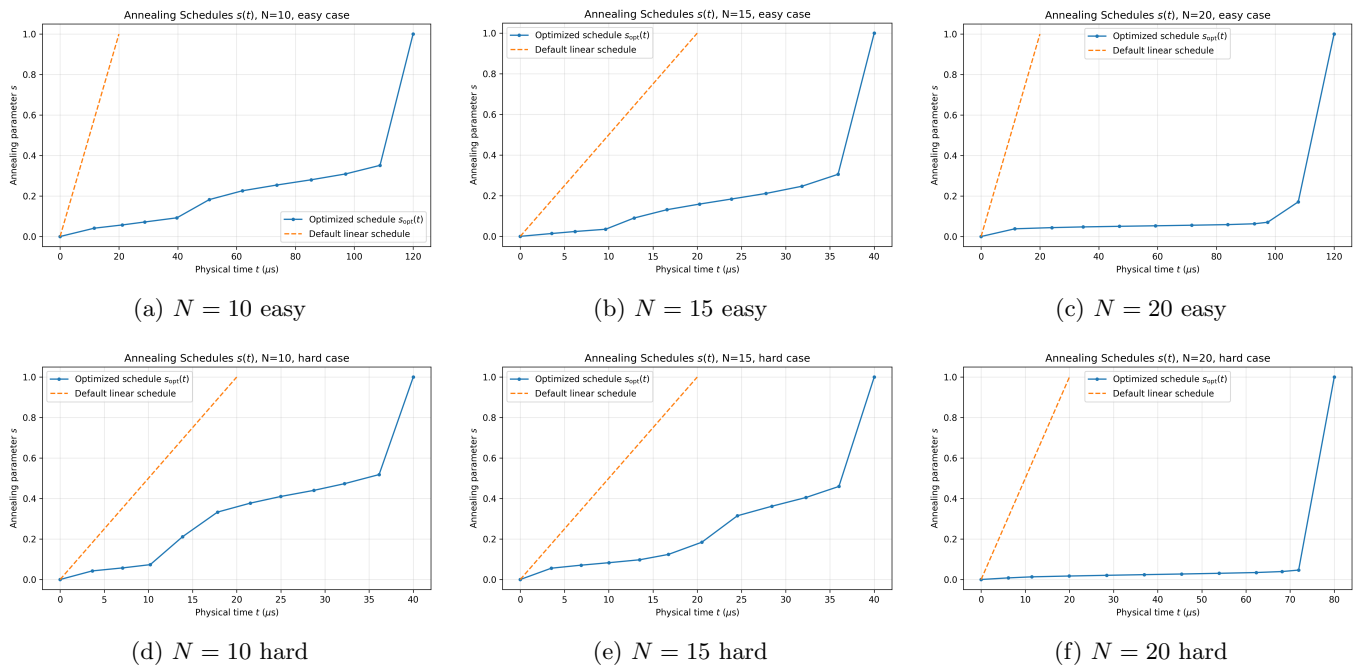


FIG. 6: Optimized annealing schedules produced by Tx-NQDT versus default annealing schedules for representative easy and hard instances at system sizes $N = 10, 15, 20$.

tional efficiency. In our experiments, this strategy reduced per- s training wall time by approximately 53% relative to random reinitialization. This behavior is consistent with physical intuition: for sufficiently small Δs , instantaneous eigenstates vary smoothly, so a shared transformer backbone with lightweight output-head updates suffices to track the evolving spectrum.

By providing direct access to $E_0(s)$, $E_1(s)$, and the transition matrix element $\langle \psi_1(s) | \frac{dH}{ds} | \psi_0(s) \rangle$, Tx-NQDT integrates naturally with first-order adiabatic perturbation theory (FOAPT). The resulting adiabatic control functional $\Lambda(s)$ can be integrated to construct instance-specific annealing schedules that slow down near narrow gaps and accelerate where the spectrum is benign. Crucially, schedule synthesis becomes a lightweight post-processing step once the spectrum has been learned on a

coarse s -grid, without requiring repeated diagonalization or hardware-in-the-loop tuning. This property makes the approach particularly attractive for hardware-oriented workflows, where factory-provided $A(s)$ and $B(s)$ curves can be retained and only the logical time rescaling is modified.

The empirical experiments on the D-Wave Advantage system provide a concrete end-to-end validation of this pipeline. Across randomly generated QUBO instances at $N = 10, 15$, and 20 , Tx-NQDT-informed schedules consistently outperform the device’s default linear schedule, improving ground-state success probability for a majority of instances in both easy and hard subsets. The observed gains align closely with FOAPT diagnostics derived from Tx-NQDT, confirming that allocating additional anneal time to narrow-gap regions is bene-

ficial even in the presence of hardware noise, calibration drift, and strict control-point constraints. While the magnitude of improvement naturally decreases with system size—reflecting longer embeddings, increased chain fragility, and stronger open-system effects—the persistence of schedule-level gains at $N = 20$ demonstrates that spectrum-aware control remains effective beyond the regime where exact spectral information is accessible.

The FOAPT-based rescaling rests on an important assumption: that the physical device follows the modified schedule closely enough that the instantaneous Hamiltonian remains well approximated by $H_{\text{QA}}(s)$ with the same $A(s)$ and $B(s)$ used during training. In practice, calibration errors, decoherence, control bandwidth, and extremely small spectral gaps can limit the quantitative validity of first-order perturbation theory. Indeed, when

$$\frac{|\langle \psi_1(s) | \frac{dH}{ds} | \psi_0(s) \rangle|}{\Delta(s)^2} \quad (31)$$

becomes large, FOAPT may formally predict excitation probabilities exceeding unity, signaling a breakdown of the linear-response regime. In such cases, FOAPT should be interpreted diagnostically rather than literally: it still reliably identifies the dangerous s -windows where additional dwell time is warranted, even if the numerical value of the estimate is no longer meaningful.

Beyond schedule construction, Tx-NQDT provides a general-purpose tool for probing annealing landscapes. The learned gap curves $\Delta(s)$ enable identification of avoided crossings, statistical studies of disorder-induced gap distributions, and targeted flagging of instances that merit more expensive exact treatment. This capability connects naturally to many-body diagnostics, where gap closings along a control path often signal quantum critical behavior or localization phenomena. Because the transformer operates with masked attention on the coupling graph, its computational cost scales with the number of edges $|E|$ rather than the Hilbert-space dimension. For sparse graphs, this yields near-linear scaling in N , suggesting that the framework can be extended to larger simulated embeddings and broader disorder ensembles without qualitative changes to the algorithm.

An additional strength of the framework is the closed-loop consistency between spectrum learning and control validation. Given a candidate schedule $s(t)$ and the learned instantaneous eigenstates, the same FOAPT expressions used to design the schedule can be re-evaluated along the trajectory to verify that slow-down regions coincide with large transition amplitudes. If residual FOAPT indicators remain large after schedule refinement, this points to a fundamentally small gap rather than an overly aggressive schedule. This feedback loop provides a principled way to distinguish spectral limitations from control limitations.

Looking ahead, several directions emerge naturally from this work. On the modeling side, extending Tx-NQDT beyond transverse-field Ising Hamiltonians will test the generality of the masked-attention inductive bias.

Exploring alternative neural quantum state representations—such as autoregressive flows, equivariant graph networks, or diffusion-based samplers—may further reduce variance near small gaps and improve excited-state stability. On the control side, incorporating uncertainty quantification into the learned spectra could enable risk-aware schedule design that explicitly trades off speed against robustness. Finally, combining Tx-NQDT-derived schedules with additional hardware primitives—such as pauses, reverse annealing, or local anneal offsets—offers a promising route to further performance gains. More broadly, the demonstrated ability to close the loop from neural spectral reconstruction to hardware-compatible control suggests that digital twins like Tx-NQDT could become standard front-end tools for quantum annealing experiments, enabling principled, instance-adaptive control without exhaustive hardware-side tuning.

ACKNOWLEDGMENTS

J. Lu respectfully acknowledges the late Associate Professor Stéphane Bressan for his valuable discussions. This research project is supported by the National Research Foundation Singapore under its Industry Alignment Fund – Pre-positioning (IAF-PP) Funding Initiative, and the Monetary Authority of Singapore under A-0003504-17-00. Any opinions, findings and conclusions or recommendations expressed in this material are those of the authors and do not reflect the views of National Research Foundation, Singapore, or of the Monetary Authority of Singapore.

Appendix A: Adiabatic Theorem

As a fundamental result of quantum mechanics, adiabatic theorem can be found in most quantum mechanics textbooks, although the exact formulation may be more or less different. Here we follow the expression in J. J. Sakurai and Jim Napolitano’s *Modern Quantum Mechanics* [34].

Given a time-dependent quantum system with Hamiltonian $H(t)$, the Schrödinger equation can be written as

$$i\hbar \frac{\partial}{\partial t} |\alpha(t)\rangle = H(t) |\alpha(t)\rangle. \quad (\text{A1})$$

The general solution $|\alpha(t)\rangle$ can be decomposed into a linear combination of the time-dependent eigenstates $|n(t)\rangle$ of $H(t)$ as follows,

$$|\alpha(t)\rangle = \sum_n c_n(t) e^{i\theta_n(t)} |n(t)\rangle, \quad (\text{A2})$$

where

$$\theta_n(t) \equiv -\frac{1}{\hbar} \int_0^t E_n(t') dt' \quad (\text{A3})$$

with $E_n(t)$ being the n -th eigenvalue of $H(t)$.

The time evolution of the m -th coefficient c_m is then

$$\begin{aligned} \frac{dc_m}{dt} &= -c_m(t) \langle m(t) | \frac{\partial}{\partial t} | m(t) \rangle \\ &\quad - \sum_n c_n(t) e^{i(\theta_n - \theta_m)} \frac{\langle m(t) | \frac{dH}{dt} | n(t) \rangle}{E_n - E_m}. \end{aligned} \quad (\text{A4})$$

The second term in the above equation is responsible for the mixing of the n -th eigenstate and the m -th eigenstate with $n \neq m$, which can be neglected if the following condition of adiabatic approximation is satisfied:

$$\left| \frac{\langle m(t) | \frac{dH}{dt} | n(t) \rangle}{E_n(t) - E_m(t)} \right| \ll \left| \langle m(t) | \frac{\partial}{\partial t} | m(t) \rangle \right| \sim \left| \frac{E_m(t)}{\hbar} \right|. \quad (\text{A5})$$

The quantity $\left| \frac{\langle m(t) | \frac{dH}{dt} | n(t) \rangle}{E_n(t) - E_m(t)} \right|$ represents the inverse of the time scale for changes in the Hamiltonian $H(t)$.

Appendix B: Proof of the Brauer Theorem and a Relevant Corollary

In linear algebra, Brauer theorem [32], given in Theorem 1 as the version for Hermitian matrices, can be used to approximate the non-extreme eigenvectors and eigenvalues of an Hermitian matrix by shifting the extreme eigenvalues.

Theorem 1. Let H be an $n \times n$ Hermitian matrix with eigenvalues $\lambda_1 \leq \dots \leq \lambda_n$. Let \mathbf{u}_i be the corresponding eigenvector of H with eigenvalue λ_i . Let \mathbf{v} be any n -dimensional column vector. Then, the matrix $\tilde{H} = H + \mathbf{u}_i \mathbf{v}^\dagger$ has eigenvalues $\lambda_1, \dots, \lambda_i + \mathbf{v}^\dagger \mathbf{u}_i, \dots, \lambda_m$. Moreover, the eigenvector \mathbf{x}_i does not change, i.e. $\tilde{H} \mathbf{u}_i = (\lambda_i + \mathbf{v}^\dagger \mathbf{u}_i) \mathbf{u}_i$.

Proof. Without loss of generality, we choose $i = 1$. Then with the normalized eigenvector \mathbf{u}_1 there exist a non-singular $n \times n$ matrix $A = \begin{pmatrix} \mathbf{u}_1 & \Omega \end{pmatrix}$, where Ω is some $n \times (n-1)$ matrix. The inverse matrix of A is denoted by $A^{-1} = \begin{pmatrix} \mathbf{w} \\ \Gamma \end{pmatrix}$, in which \mathbf{w} is a $1 \times n$ matrix and Γ is an $(n-1) \times n$ matrix. Note that, from $A^{-1}A = \mathbb{I}_n$, we have $\mathbf{w} \mathbf{u}_1 = \mathbb{I}_1 = 1$ and $\Gamma \mathbf{u}_1 = \mathbf{0}_{(n-1) \times 1}$ with $\mathbf{0}_{(n-1) \times 1}$ being the $(n-1) \times 1$ zero matrix.

Then one has

$$\begin{aligned} A^{-1}HA &= \begin{pmatrix} \mathbf{w} \\ \Gamma \end{pmatrix} H \begin{pmatrix} \mathbf{u}_1 & \Omega \end{pmatrix} \\ &= \begin{pmatrix} \mathbf{w} \\ \Gamma \end{pmatrix} \begin{pmatrix} \lambda_1 \mathbf{u}_1 & H\Omega \end{pmatrix} \\ &= \begin{pmatrix} \lambda_1 \mathbf{w} \mathbf{u}_1 & \mathbf{w} H \Omega \\ \lambda_1 \Gamma \mathbf{u}_1 & \Gamma H \Omega \end{pmatrix} \\ &= \begin{pmatrix} \lambda_1 & \mathbf{w} H \Omega \\ \mathbf{0}_{(n-1) \times 1} & \Gamma H \Omega \end{pmatrix}. \end{aligned} \quad (\text{B1})$$

Because H and $A^{-1}HA$ have the same set of eigenvalues, we immediately find that the set of eigenvalue of $\Gamma H \Omega$ is $\{\lambda_2, \dots, \lambda_n\}$.

For an arbitrary n -dimensional column vector \mathbf{v} , one has

$$\begin{aligned} A^{-1}(H + \mathbf{u}_1 \mathbf{v}^\dagger)A &= A^{-1}HA + A^{-1} \mathbf{u}_1 \mathbf{v}^\dagger A \\ &= \begin{pmatrix} \lambda_1 + \mathbf{w} \mathbf{u}_1 \mathbf{v}^\dagger \mathbf{u}_1 & \mathbf{w} H \Omega + \mathbf{w} \mathbf{u}_1 \mathbf{v}^\dagger \Omega \\ \mathbf{0}_{(n-1) \times 1} + \Gamma \mathbf{u}_1 \mathbf{v}^\dagger \mathbf{u}_1 & \Gamma H \Omega + \Gamma \mathbf{u}_1 \mathbf{v}^\dagger \Omega \end{pmatrix}. \end{aligned} \quad (\text{B2})$$

Again, by making use of $\mathbf{w} \mathbf{u}_1 = \mathbb{I}_1 = 1$ and $\Gamma \mathbf{u}_1 = \mathbf{0}_{(n-1) \times 1}$, we have

$$A^{-1}(H + \mathbf{u}_1 \mathbf{v}^\dagger)A = \begin{pmatrix} \lambda_1 + \mathbf{v}^\dagger \mathbf{u}_1 & \mathbf{w} H \Omega + \mathbf{v}^\dagger \Omega \\ \mathbf{0}_{(n-1) \times 1} & \Gamma H \Omega \end{pmatrix}. \quad (\text{B3})$$

The set of eigenvalues of $H + \mathbf{u}_1 \mathbf{v}^\dagger$ is the same as that of $A^{-1}(H + \mathbf{u}_1 \mathbf{v}^\dagger)A$, which is the union of $\{\lambda_1 + \mathbf{v}^\dagger \mathbf{u}_1\}$ and the set of eigenvalues of $\Gamma H \Omega$, i.e., $\{\lambda_1 + \mathbf{v}^\dagger \mathbf{u}_1, \lambda_2, \dots, \lambda_n\}$. It is also easy to see that the eigenvalue $\lambda_1 + \mathbf{v}^\dagger \mathbf{u}_1$ corresponds to the eigenvector \mathbf{u}_1 .

Hence, we have completed the proof of the above theorem. \square

Corollary 1. Let H be an $n \times n$ Hermitian matrix with eigenvalues $\lambda_1 \leq \dots \leq \lambda_n$. Let \mathbf{u}_i be the corresponding **normalized** eigenvector of H with the eigenvalue λ_i . Then, the matrix $\tilde{H} = H + \delta \cdot \mathbf{u}_i \mathbf{u}_i^\dagger$ has eigenvalues $\lambda_1, \dots, \lambda_i + \delta, \dots, \lambda_n$, with the same set of eigenvectors as H .

Proof. The above assertion follows directly from Theorem 1, together with the fact that the set $\{\mathbf{u}_1, \dots, \mathbf{u}_n\}$ forms an orthonormal basis of eigenvectors for the matrix H . \square

Appendix C: Optimized Annealing Schedule Construction

This appendix describes the concrete procedure we use to turn Tx-NQDT spectral estimates into a time-parameterized annealing schedule $s(t)$. The objective is to obtain a trajectory that (i) slows down automatically near instance-specific small gaps, (ii) respects a hardware-style bound on the ramp rate, and (iii) stays compatible with the standard Hamiltonian

$$\begin{aligned} H_{\text{QA}}(s) &= -\frac{A(s)}{2} \sum_i \hat{\sigma}_x^{(i)} \\ &\quad + \frac{B(s)}{2} \left(\sum_i h_i \hat{\sigma}_z^{(i)} + \sum_{i>j} J_{ij} \hat{\sigma}_z^{(i)} \hat{\sigma}_z^{(j)} \right), \end{aligned} \quad (\text{C1})$$

with $s \in [0, 1]$ and hardware control curves $A(s), B(s)$.

1. FOAPT control functional

On a discrete grid $\{s_r\}_{r=0}^R \subset [0, 1]$, Tx-NQDT provides the instantaneous ground and first-excited states $|\Psi_0(s_r)\rangle, |\Psi_1(s_r)\rangle$ and their eigenenergies $E_0(s_r), E_1(s_r)$. We also estimate the transition matrix element

$$M_{01}(s_r) = \langle \Psi_0(s_r) | \frac{dH_{QA}}{ds}(s_r) | \Psi_1(s_r) \rangle, \quad (C2)$$

where $\frac{dH_{QA}}{ds}(s)$ is computed analytically from the known $A(s), B(s)$.

Following the FOAPT derivation, we define the control functional

$$\Lambda(s_r) = \frac{|\langle \Psi_0(s_r) | \frac{dH_{QA}}{ds}(s_r) | \Psi_1(s_r) \rangle|}{|E_1(s_r) - E_0(s_r)|^2} = \frac{|M_{01}(s_r)|}{\Delta(s_r)^2}, \quad (C3)$$

with $\Delta(s_r) = E_1(s_r) - E_0(s_r)$. Large values of $\Lambda(s)$ indicate regions where the evolution should slow down to suppress diabatic transitions.

2. Equal-mass knot placement in s

We now compress the grid $\{s_r\}$ into a small set of breakpoints

$$0 = s_0 < s_1 < \dots < s_K = 1,$$

such that each interval carries the same FOAPT ‘‘mass.’’ Define the cumulative integral

$$F(s) = \int_0^s \Lambda(u) du, \quad (C4)$$

approximated numerically on the discrete samples. Let $F(1)$ be the total mass. We choose knots by solving

$$F(s_k) = \frac{k}{K} F(1), \quad k = 0, 1, \dots, K. \quad (C5)$$

This places more knots where $\Lambda(s)$ is large (small gaps, strong couplings) and fewer knots where the system is easy. In our experiments we take $K \approx 12$ so that the final $s(t)$ is a modest piecewise-linear curve.

3. Time-parameterization with a slope cap

Let the total annealing time be $T > 0$. For each segment $[s_k, s_{k+1}]$ define its length

$$\Delta s_k = s_{k+1} - s_k. \quad (C6)$$

We wish to assign a duration Δt_k to each segment so that (i) segments with large FOAPT weight get more time, and (ii) the ramp rate is bounded:

$$\frac{ds}{dt} \leq \gamma_{\max}. \quad (C7)$$

In the experiments we use $\gamma_{\max} = 2.0 (\mu s)^{-1}$.

a. Minimal feasible time. The slope cap (C7) implies the per-segment lower bound

$$\Delta t_k^{\min} = \frac{\Delta s_k}{\gamma_{\max}}. \quad (C8)$$

Summing over segments gives $\sum_k \Delta t_k^{\min}$, the minimal total time compatible with the cap. If $\sum_k \Delta t_k^{\min} > T$, we uniformly scale these minimal durations by $T / \sum_k \Delta t_k^{\min}$.

b. FOAPT-proportional time. Ignoring the cap, FOAPT would allocate time proportionally to

$$\Delta t_k^{\text{FOAPT}} \propto \Delta s_k \bar{\Lambda}_k, \quad \bar{\Lambda}_k \approx \frac{1}{\Delta s_k} \int_{s_k}^{s_{k+1}} \Lambda(u) du, \quad (C9)$$

and then normalize so that $\sum_k \Delta t_k^{\text{FOAPT}} = T$.

c. Blending the two. When $\sum_k \Delta t_k^{\min} \leq T$, we distribute the remaining time

$$T - \sum_k \Delta t_k^{\min}$$

across segments in proportion to the positive ‘‘slack’’

$$w_k = \max(\Delta t_k^{\text{FOAPT}} - \Delta t_k^{\min}, 0). \quad (C10)$$

If $\sum_k w_k > 0$, we set

$$\Delta t_k = \Delta t_k^{\min} + \left(T - \sum_j \Delta t_j^{\min} \right) \frac{w_k}{\sum_j w_j}, \quad (C11)$$

otherwise we distribute the remainder evenly. By construction, every segment obeys

$$\frac{\Delta s_k}{\Delta t_k} \leq \gamma_{\max} \quad (C12)$$

and the total time is exactly T .

Finally we build time knots

$$t_0 = 0, \quad t_{k+1} = t_k + \Delta t_k, \quad k = 0, \dots, K-1, \quad (C13)$$

and define $s(t)$ on each interval $[t_k, t_{k+1}]$ by linear interpolation:

$$s(t) = s_k + \frac{s_{k+1} - s_k}{t_{k+1} - t_k} (t - t_k), \quad t \in [t_k, t_{k+1}]. \quad (C14)$$

4. Export to hardware-style controls

Given $s(t)$, the physical control signals are obtained by composition

$$A(t) = A(s(t)), \quad B(t) = B(s(t)), \quad t \in [0, T], \quad (C15)$$

so the device executes the same Hamiltonian family but with an instance-aware, nonlinear re-timing of the anneal parameter. Because the number of segments is small and all slopes satisfy (C7), the schedule can be tabulated and uploaded directly.

5. Summary

The overall schedule construction is:

1. **Spectral estimation:** use Tx-NQDT to obtain $E_0(s_r)$, $E_1(s_r)$ and $M_{01}(s_r)$.
2. **Control functional:** compute $\Lambda(s_r) = |M_{01}(s_r)|/\Delta(s_r)^2$.
3. **Equal-mass knots:** choose $\{s_k\}_{k=0}^K$ such that each interval integrates the same FOAPT mass.
4. **Time-parameterization with slope cap:** assign $\{\Delta t_k\}$ via (C11), guaranteeing $\frac{ds}{dt} \leq \gamma_{\max}$ and $\sum_k \Delta t_k = T$.

This is the procedure used in our experiments to generate instance-specific, FOAPT-guided annealing schedules from the Tx-NQDT outputs.

Appendix D: First-Order Adiabatic Perturbation Theory

The adiabatic theorem states that a quantum system prepared in an instantaneous eigenstate of a slowly varying Hamiltonian will remain in that eigenstate (up to phase) provided the evolution is sufficiently slow and energy-level crossings are avoided. In realistic annealing settings, however, the total time is finite and small spectral gaps make the ideal condition hard to satisfy, so transitions to low-lying excited states can occur. First-order adiabatic perturbation theory (FOAPT) gives a simple, quantitative estimate of such transitions, and it is the model we use to score candidate schedules $s(t)$.

Throughout this appendix we make two standard assumptions: (i) the spectrum of the instantaneous Hamiltonian is non-degenerate along the path, and (ii) a single transition, typically from the ground state to the first excited state, dominates the error. Under these assumptions FOAPT is accurate enough to guide schedule design.

1. Setup and notation

In the main text the annealing Hamiltonian is parameterized as

$$H(s) \equiv H_{\text{QA}}(s) = -\frac{A(s)}{2} \sum_i \hat{\sigma}_x^{(i)} + \frac{B(s)}{2} \left(\sum_i h_i \hat{\sigma}_z^{(i)} + \sum_{i>j} J_{ij} \hat{\sigma}_z^{(i)} \hat{\sigma}_z^{(j)} \right), \quad (\text{D1})$$

with a dimensionless anneal parameter $s \in [0, 1]$. The physical time $t \in [0, T]$ enters only through a schedule

$s(t)$, so $H(t) = H(s(t))$ and

$$\frac{dH}{dt} = \frac{dH}{ds} \frac{ds}{dt}. \quad (\text{D2})$$

Let $\{|\psi_k(s)\rangle\}$ and $\{E_k(s)\}$ be the instantaneous eigenstates and eigenvalues of $H(s)$,

$$H(s)|\psi_k(s)\rangle = E_k(s)|\psi_k(s)\rangle, \quad k = 0, 1, 2, \dots \quad (\text{D3})$$

with the ordering $E_0(s) \leq E_1(s) \leq \dots$ as in Sec. 2.

2. FOAPT expression

Consider the time-dependent Schrödinger equation

$$i \frac{d}{dt} |\Psi(t)\rangle = H(s(t)) |\Psi(t)\rangle, \quad (\text{D4})$$

with the system initialized in the ground state, $|\Psi(0)\rangle = |\psi_0(s(0))\rangle$. FOAPT expands $|\Psi(t)\rangle$ in the instantaneous basis and keeps only the leading non-adiabatic term. For the transition from the ground state to a specific excited state $|\psi_1\rangle$ this gives the familiar amplitude

$$c_{0 \rightarrow 1}^{(1)}(T) = - \int_0^T \frac{\langle \psi_1(t) | \dot{H}(t) | \psi_0(t) \rangle}{E_1(t) - E_0(t)} e^{i \int_0^t (E_1(t') - E_0(t')) dt'} dt, \quad (\text{D5})$$

where dots denote derivatives with respect to physical time t . The corresponding transition probability is

$$P_{0 \rightarrow 1} = |c_{0 \rightarrow 1}^{(1)}(T)|^2. \quad (\text{D6})$$

Using (D2) and changing variables from t to s we obtain the form used in the main text:

$$c_{0 \rightarrow 1}^{(1)}(T) = - \int_0^1 \frac{\langle \psi_1(s) | \frac{dH}{ds} | \psi_0(s) \rangle}{E_1(s) - E_0(s)} \frac{ds}{\dot{s}(s)} e^{i \int_0^s \frac{E_1(s') - E_0(s')}{\dot{s}(s')} ds'} ds, \quad (\text{D7})$$

where $\dot{s}(s) \equiv \frac{ds}{dt}$ evaluated at the point with anneal parameter s . Equation (D7) shows explicitly what the schedule controls: making $\dot{s}(s)$ small in regions where the matrix element is large or where the gap $E_1(s) - E_0(s)$ is small suppresses the transition.

For convenience we introduce the *local adiabatic difficulty*

$$\Lambda(s) \equiv \frac{|\langle \psi_1(s) | \frac{dH}{ds} | \psi_0(s) \rangle|}{(E_1(s) - E_0(s))^2}, \quad (\text{D8})$$

which is exactly the quantity our Tx-NQDT estimates in Sec. 2.4. Up to phases, FOAPT says that $P_{0 \rightarrow 1}$ scales like the squared, time-integrated $\Lambda(s)\dot{s}(s)$.

3. Piecewise-linear schedules

In experiments we use piecewise-linear schedules,

$$s(t) = s_i + \frac{s_{i+1} - s_i}{t_{i+1} - t_i} (t - t_i), \quad t \in [t_i, t_{i+1}], \quad (\text{D9})$$

with $0 = t_0 < t_1 < \dots < t_K = T$ and $0 = s_0 < s_1 < \dots < s_K = 1$. On each segment i the slope

$$\dot{s}_i = \frac{s_{i+1} - s_i}{t_{i+1} - t_i} \quad (\text{D10})$$

is constant, so (D7) decomposes into a sum of K integrals,

$$c_{0 \rightarrow 1}^{(1)}(T) = - \sum_{i=0}^{K-1} \int_{s_i}^{s_{i+1}} \frac{\langle \psi_1(s) | \frac{dH}{ds} | \psi_0(s) \rangle}{E_1(s) - E_0(s)} \frac{1}{\dot{s}_i} e^{i\phi_i(s)} ds, \quad (\text{D11})$$

where $\phi_i(s)$ is the accumulated dynamical phase up to s on segment i . Because \dot{s}_i is constant, each segment contributes roughly in proportion to

$$\frac{1}{\dot{s}_i} \int_{s_i}^{s_{i+1}} \Lambda(s) ds, \quad (\text{D12})$$

which motivates the *equal-mass* construction used in the main text: we choose the breakpoints $\{s_i\}$ so that the integral of $\Lambda(s)$ over every segment is the same, and then set the times $\{t_i\}$ so that device-level slope constraints (e.g. $\dot{s}_i \leq 2 \mu\text{s}^{-1}$) are satisfied.

This structure is also what allows us to insert Tx-NQDT predictions directly: once $E_0(s)$, $E_1(s)$ and the matrix element are available on a dense grid (from Secs. 2.2–2.3), all terms in (D11) can be evaluated numerically with trapezoidal or Simpson rules.

4. What FOAPT does and does not capture

FOAPT is a first-order estimate. It captures:

- the correct scaling of transitions with the inverse gap;
- the effect of schedule slowdowns near small gaps;
- interference between segments through the phase factors $\phi_i(s)$.

It does *not* capture higher-order multilevel effects or level crossings. In our workflow we use FOAPT only as a *control functional* to rank candidate piecewise-linear schedules that already respect hardware slope limits. The actual schedules are then tested numerically with the Tx-NQDT model itself, as described in Sec. 2.4.

Appendix E: Time Complexity Analysis and Comparison with Exact Diagonalization

This appendix summarizes the computational cost of the proposed transformer-based neural quantum digital twin (Tx-NQDT) pipeline and contrasts it with exact diagonalization (ED). The goal is to make clear (i) where the exponential bottleneck of ED appears, (ii) how Tx-NQDT avoids it by exploiting graph sparsity and transfer along the anneal parameter, and (iii) what terms dominate the wall time in practice.

1. Exact diagonalization

For a system of N qubits/spins the Hilbert space has dimension 2^N . A straightforward ED of an $H(s) \in \mathbb{C}^{2^N \times 2^N}$ Hamiltonian requires

- memory $\mathcal{O}(2^N)$ just to store state vectors, and up to $\mathcal{O}(4^N)$ to store dense Hamiltonians;
- time $\mathcal{O}(2^{3N})$ for naive dense eigensolvers, or $\mathcal{O}(2^{2N})$ when using sparse structure and iterative solvers for only the lowest eigenpairs.

Even with sparse Krylov or Lanczos methods, the cost grows exponentially in N because each matrix–vector multiplication touches $\Theta(2^N)$ entries. Moreover, annealing studies typically require spectra at multiple values s_1, \dots, s_{n_s} , so ED must be repeated n_s times, yielding an overall scaling of

$$T_{\text{ED}} = \mathcal{O}(n_s 2^{2N}) \quad (\text{iterative, low eigenpairs}). \quad (\text{E1})$$

This restricts ED to $N \lesssim 16$ – 20 in practice, depending on symmetry and available memory, and makes per-instance schedule optimization infeasible for larger problems.

2. Tx-NQDT forward/training cost at a fixed s

Let N be the number of spins, $|E|$ the number of nonzero couplings in the QUBO/Ising graph, L the number of transformer blocks, and d the model (token) dimension. Section 2.2 uses *graph-masked* multi-head attention, so one forward pass through the backbone has cost

$$T_{\text{fwd}}(N, |E|) = \mathcal{O}(L(Nd^2 + |E|d)), \quad (\text{E2})$$

where the Nd^2 term comes from the tokenwise feedforward layers and the $|E|d$ term comes from attention restricted to edges (optionally expanded to k -hop neighborhoods, in which case $|E|$ should be read as the number of masked edges). On sparse hardware graphs (Pegasus/Chimera) we have $|E| = \Theta(N)$, so (E2) becomes nearly linear in N :

$$T_{\text{fwd}}(N) = \mathcal{O}(LN d^2). \quad (\text{E3})$$

Training at a fixed s is variational Monte Carlo (VMC): we draw M samples $x^{(1)}, \dots, x^{(M)} \sim |\Psi_\theta(\cdot; s)|^2$, evaluate local energies, and backpropagate. Ignoring sampler autocorrelation, one epoch has cost

$$T_{\text{train}}(s) = \mathcal{O}(M T_{\text{fwd}}(N)) = \mathcal{O}(MLN d^2). \quad (\text{E4})$$

Because we use a variance-based stopping rule, the number of epochs at “easy” s (large gap, small $\Lambda(s)$) is small, while near small gaps more epochs are taken automatically. This produces a data-dependent constant factor but does not change the polynomial scaling in N .

3. Transfer along the anneal parameter

Let n_s be the number of grid points in $s \in [0, 1]$ (e.g., $n_s = 21$ in the base experiments, or a denser grid near predicted gaps). Tx-NQDT *reuses* the parameters trained at $s = s_k$ as initialization for $s = s_{k+1}$, so we do *not* pay the full training cost n_s times. If $\alpha \in (0, 1]$ denotes the average fraction of ground-state steps needed when warm-starting the next s , the total cost is

$$T_{\text{TxNQDT}} = \mathcal{O}(M L N d^2 (1 + \alpha(n_s - 1))), \quad (\text{E5})$$

with α typically well below 1 in our annealing runs because spectra vary smoothly in s . For example, $\alpha \approx 0.3$ – 0.5 is common when gaps are not closing too sharply.

4. Excited states via Brauer deflation

Section 2.3 shows that excited states are obtained by reusing the *same* backbone and attaching per-state heads, then finetuning on a deflated Hamiltonian. If K_{exc} low-lying states are required, the additional cost is roughly

$$T_{\text{exc}} = \mathcal{O}(K_{\text{exc}} \beta M L N d^2), \quad (\text{E6})$$

where $\beta < 1$ is a finetuning factor (we train excited-state heads for only 20–60% of ground-state steps). Crucially, the *backbone* cost is not multiplied by K_{exc} ; only the lightweight heads are.

5. Cost of FOAPT-driven schedule construction

Once Tx-NQDT has already produced $\{E_0(s_j), E_1(s_j), \langle \psi_1(s_j) | \frac{dH}{ds} | \psi_0(s_j) \rangle\}_{j=1}^{n_s}$ on a grid, the FOAPT control functional

$$\Lambda(s_j) = \frac{|\langle \psi_1(s_j) | \frac{dH}{ds} | \psi_0(s_j) \rangle|}{(E_1(s_j) - E_0(s_j))^2} \quad (\text{E7})$$

is evaluated in $\mathcal{O}(n_s)$ time. Building a piecewise-linear equal-mass schedule with K segments is also $\mathcal{O}(n_s + K)$ (a single cumulative sum plus interpolation). Therefore the schedule-synthesis stage is *negligible* compared to learning the spectrum:

$$T_{\text{schedule}} = \mathcal{O}(n_s + K) \ll T_{\text{TxNQDT}}. \quad (\text{E8})$$

6. Comparison and discussion

Putting (E1) and (E5) side by side,

$$T_{\text{ED}} = \mathcal{O}(n_s 2^{2N}), \quad (\text{E9})$$

$$T_{\text{TxNQDT}} = \mathcal{O}(M L N d^2 (1 + \alpha(n_s - 1))), \quad (\text{E10})$$

we see that ED becomes prohibitive once N grows, even for moderate n_s , whereas Tx-NQDT grows *polynomially* in N and *linearly* in n_s (up to the warm-start factor α). This is the main reason we can train on instances with $N = 10, 15, 20$ (and potentially above) while still sweeping multiple anneal times and schedules, something infeasible with ED.

Two caveats are worth noting:

1. The VMC cost hides sampler autocorrelation. If the Markov chain mixes slowly near small gaps, the *effective* M must be increased, inflating the constant in (E4). This is precisely why we add independent proposals and variance-based stopping in the main text.
2. For very small N (e.g., $N \leq 10$), ED may still be faster *per* s than training a transformer. In those regimes we in fact *use* ED to validate Tx-NQDT, not to replace it.

Overall, the transformer formulation reduces the core cost from exponential (ED) to polynomial in N : it is near-linear in N only when the coupling graph is sparse ($|E| = \mathcal{O}(N)$), while for dense graphs such as our RHM ($|E| = \mathcal{O}(N^2)$) the attention term scales quadratically.

Appendix F: Criteria for Schedule Optimization under Hardware Constraint

We work with a FOAPT-aligned control functional evaluated on a dense grid in $s \in [0, 1]$ and then project it to a device-realizable piecewise-linear schedule with at most twelve control points. Let $\Lambda(s)$ denote the selected adiabatic “difficulty” measure along the path, for example

$$\Lambda_{\text{FOAPT}}(s) = \frac{|\langle \Psi_1(s) | \frac{dH}{ds} | \Psi_0(s) \rangle|}{(E_1(s) - E_0(s))^2}, \quad (\text{F1})$$

where $|\Psi_0(s)\rangle, |\Psi_1(s)\rangle$ and $E_0(s), E_1(s)$ come from the Tx-NQDT at the same s . The continuous FOAPT control law prescribes

$$\frac{ds}{dt} = \frac{C}{\Lambda(s)}, \quad \int_0^1 \Lambda(s) ds = CT, \quad (\text{F2})$$

with T the total anneal time and C the normalization constant. This law says: evolve slowly where $\Lambda(s)$ is large (small gap, large transition matrix element) and faster where it is small.

However, real quantum annealers accept only a small number of time-value pairs $\{(t_k, s_k)\}_{k=0}^K$ (typically $K \leq 11$ so we get at most 12 points), require $0 = t_0 < t_1 < \dots < t_K = T$, and require $0 = s_0 < s_1 < \dots < s_K = 1$. We therefore need a principled projection from the continuous law in (F2) to such a constrained schedule.

1. Step 1: Equal-mass knot selection

Define the cumulative difficulty

$$F(s) = \int_0^s \Lambda(u) du, \quad F(1) = \int_0^1 \Lambda(u) du. \quad (\text{F3})$$

To preserve where the continuous law “spends time,” we choose the K interior knots by the equal-mass rule

$$s_k = F^{-1}\left(\frac{k}{K}F(1)\right), \quad k = 0, 1, \dots, K, \quad (\text{F4})$$

with $s_0 = 0$ and $s_K = 1$. Each segment $[s_k, s_{k+1}]$ therefore carries the same integrated difficulty as measured by Λ . This concentrates control points automatically near small spectral gaps or large matrix elements, and keeps K modest (e.g., $K = 12$).

2. Step 2: Segmentwise speed from averaged difficulty

Within segment k we approximate $\Lambda(s)$ by its average

$$\bar{\Lambda}_k = \frac{1}{\Delta s_k} \int_{s_k}^{s_{k+1}} \Lambda(u) du, \quad \Delta s_k = s_{k+1} - s_k, \quad (\text{F5})$$

and we assign a constant speed on that segment according to the same FOAPT principle,

$$\left(\frac{ds}{dt}\right)_k = \frac{C}{\bar{\Lambda}_k}. \quad (\text{F6})$$

This immediately gives the segment duration

$$\Delta t_k = \frac{\Delta s_k}{(ds/dt)_k} = \frac{\Delta s_k \bar{\Lambda}_k}{C}. \quad (\text{F7})$$

To satisfy the global runtime constraint we pick

$$C = \frac{\sum_{k=0}^{K-1} \Delta s_k \bar{\Lambda}_k}{T}, \quad (\text{F8})$$

and then set

$$t_{k+1} = t_k + \Delta t_k, \quad t_0 = 0. \quad (\text{F9})$$

At this point we have a monotone, piecewise-linear schedule $s(t)$ that best matches the continuous FOAPT control under a K -segment budget.

3. Step 3: Hardware-feasibility filters

D-Wave-style interfaces impose additional rules, so we explicitly enforce:

a. Monotonicity: ensure $s_{k+1} > s_k$ and $t_{k+1} > t_k$ after rounding.

b. Slope bounds: for each segment compute

$$v_k = \frac{\Delta s_k}{\Delta t_k}. \quad (\text{F10})$$

Clip to hardware limits $v_{\min} \leq v_k \leq v_{\max}$ (for the experiments in this paper we used $v_{\max} = 2.0 \mu\text{s}^{-1}$). After clipping, renormalize all Δt_k by a single factor so that $\sum_k \Delta t_k = T$ still holds.

c. Minimal dwell: enforce $\Delta t_k \geq t_{\min}$ for all k to avoid degenerate very-short segments; if some Δt_k is raised to t_{\min} , rescale the remaining segments to keep the total time fixed.

In practice we also apply a light low-pass filter to the raw $\Lambda(s)$ before computing (F4) to reduce Monte-Carlo noise originating from Tx-NQDT estimates near very small gaps; this keeps neighboring $\bar{\Lambda}_k$ from oscillating and improves schedule smoothness.

4. Optional refinement objective

The equal-mass projection already respects both the FOAPT logic and the 12-point interface. When additional improvement is needed we can refine the break-points $\{s_k\}$ and durations $\{\Delta t_k\}$ by minimizing a discrete proxy of the FOAPT transition amplitude. A common choice consistent with (F1) is

$$\mathcal{J} = \sum_{k=0}^{K-1} v_k \int_{s_k}^{s_{k+1}} \frac{|\langle \Psi_1(s) | \frac{dH}{ds} | \Psi_0(s) \rangle|}{E_1(s) - E_0(s)} ds, \quad (\text{F11})$$

or, for the local-adiabatic flattening variant,

$$\mathcal{J}_{\text{flat}} = \sum_{k=0}^{K-1} \frac{1}{v_k} \int_{s_k}^{s_{k+1}} \frac{|\langle \Psi_1(s) | \frac{dH}{ds} | \Psi_0(s) \rangle|^2}{(E_1(s) - E_0(s))^2} ds. \quad (\text{F12})$$

We then take a few projected-gradient or coordinate-descent steps on $\{s_k, \Delta t_k\}$ to reduce \mathcal{J} while reapplying the monotonicity, slope, and minimal-dwell constraints above. This keeps the schedule realizable but better aligned to the actual instance-specific spectrum.

5. Fair comparison to linear baselines

To compare fairly with the device’s built-in linear schedule, we evaluate the same FOAPT proxy (F11) (or (F12)) on both schedules under the *same* total time T and the *same* slope cap v_{\max} . When multiple narrow avoided crossings are present, we reserve a small fraction of the twelve points for each such neighborhood proportionally to the local mass of $\Lambda(s)$, which prevents the projection from collapsing two nearby crossings into one segment.

This three-step construction (equal-mass knots, averaged-segment timing, hardware filtering) is the one used in our Tx-NQDT experiments and is compatible with the schedule-construction code described in the main text.

Appendix G: Examples Trained with an MLP NNQS

This appendix reports small- N baselines obtained with a simplified multilayer perceptron (MLP) NNQS. The goal is to verify that our training pipeline and estimators are model-agnostic and to provide an external sanity check for the transformer results in the main text. We consider $N \in \{4, 6\}$ and two Hamiltonian families: the transverse-field Ising model (TFIM) and randomly generated Ising instances (RHM), each evaluated along the anneal parameter $s \in [0, 1]$ on the same grid used elsewhere. For every s we estimate ground and first-excited energies, $(E_0(s), E_1(s))$, by variational Monte Carlo (VMC) with the MLP ansatz and compare them against exact diagonalization (ED).

Figs. 7,8,9,10 illustrate representative spectra. In each panel the left y -axis shows energies while the right y -axis shows the instantaneous relative error $\text{RE}_k(s) = (E_k^{\text{MLP}}(s) - E_k^{\text{ED}}(s))/|E_k^{\text{ED}}(s)|$ for $k \in \{0, 1\}$, plotted as a percentage. The curves for E_0^{MLP} and E_1^{MLP} lie essentially on top of their ED counterparts across the entire anneal for both $N = 4$ and $N = 6$. As expected, the excited-state error shows small bumps near avoided crossings or tighter gaps, while the ground-state error remains uniformly low.

Methodologically, these runs use the same $A(s), B(s)$ schedules, sampling procedure, and variance-based stopping criterion as the transformer experiments; only the wavefunction parameterization is changed to an MLP. That the MLP reproduces ED to within sub-percent accuracy at $N = 4$ and $N = 6$ confirms that our estimators, Brauer-deflation workflow, and s -wise transfer operate correctly independent of the backbone, and it provides a transparent baseline for the transformer. In particular, the excited-state curves in Figs. 7,8,9,10 track ED smoothly across s , and the relative-error traces corroborate the intuitive trend: small increases around tighter gaps and otherwise flat profiles.

Taken together, these small- N MLP results demonstrate that our training pipeline is stable and accurate even with a low-capacity ansatz. They also motivate the transformer choice for larger N : masked attention on the interaction graph reduces cost from $\mathcal{O}(N^2)$ to roughly $\mathcal{O}(|E|)$ per layer while preserving the error levels observed here, enabling us to extend the same protocol to $N = 10, 15$ (and beyond) where ED is impractical.

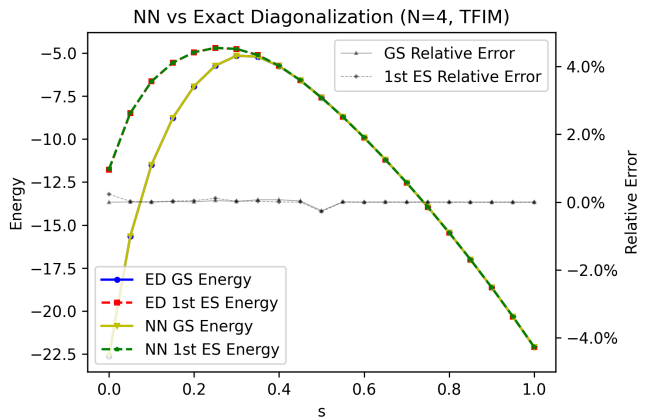


FIG. 7: Exact vs. learned spectrum for $N = 4$ (Transverse field Ising)

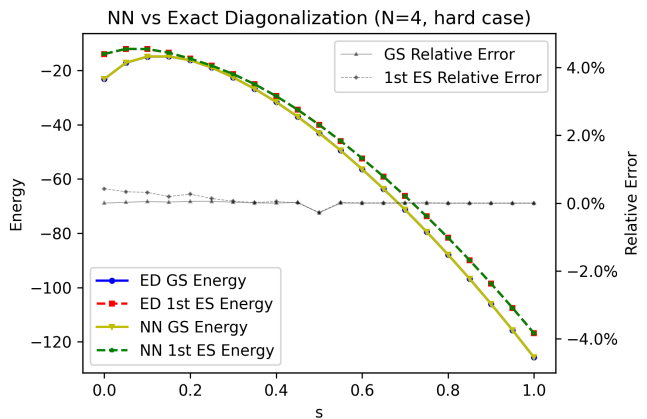


FIG. 8: Exact vs. learned spectrum for $N = 4$ (Hard case)

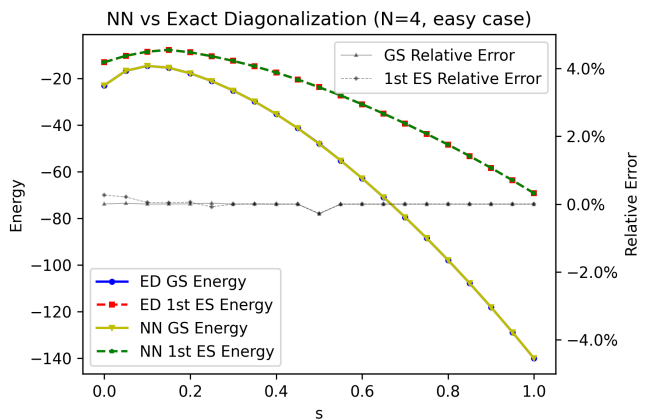


FIG. 9: Exact vs. learned spectrum for $N = 4$ (Easy case)

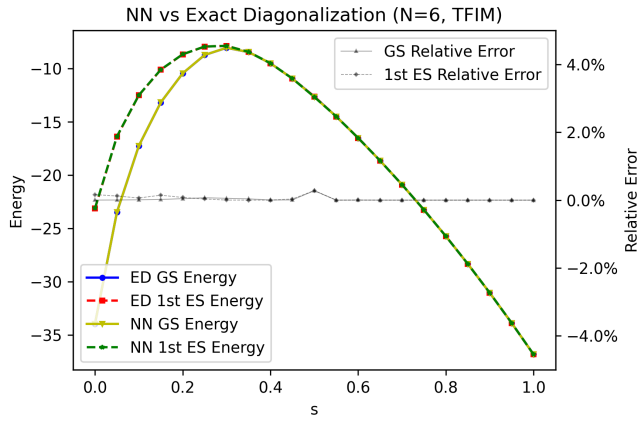


FIG. 10: Exact vs. learned spectrum for $N = 6$
(Transverse field Ising)

-
- [1] M. Cain, S. Chattopadhyay, J.-G. Liu, R. Samajdar, H. Pichler, and M. D. Lukin, Quantum speedup for combinatorial optimization with flat energy landscapes, arXiv preprint arXiv:2306.13123 (2023).
- [2] A. D. King *et al.*, Beyond-classical computation in quantum simulation, *Science* **388**, 199 (2025).
- [3] A. Rajak, S. Suzuki, A. Dutta, and B. K. Chakrabarti, Quantum annealing: an overview, *Philosophical Transactions of the Royal Society A: Mathematical, Physical and Engineering Sciences* **381**, 10.1098/rsta.2021.0417 (2022).
- [4] S. Kwon, A. Tomonaga, G. Lakshmi Bhai, S. J. Devitt, and J.-S. Tsai, Gate-based superconducting quantum computing, *Journal of Applied Physics* **129**, 10.1063/5.0029735 (2021).
- [5] S. Yarkoni, E. Raponi, T. Bäck, and S. Schmitt, Quantum annealing for industry applications: introduction and review, *Rep. Prog. Phys.* **85**, 104001 (2022).
- [6] A. Abbas *et al.*, Challenges and opportunities in quantum optimization, *Nat. Rev. Phys.* **6**, 718 (2024).
- [7] F. A. Quinton, P. A. S. Myhr, M. Barani, P. Crespo del Granado, and H. Zhang, Quantum annealing applications, challenges and limitations for optimisation problems compared to classical solvers, *Sci. Rep.* **15**, 10.1038/s41598-025-96220-2 (2025).
- [8] W. M. C. Foulkes, L. Mitas, R. J. Needs, and G. Rajagopal, Quantum monte carlo simulations of solids, *Rev. Mod. Phys.* **73**, 33 (2001).
- [9] D. M. Ceperley and B. J. Alder, Ground state of the electron gas by a stochastic method, *Phys. Rev. Lett.* **45**, 566 (1980).
- [10] M. Troyer and U.-J. Wiese, Computational complexity and fundamental limitations to fermionic quantum monte carlo simulations, *Phys. Rev. Lett.* **94**, 170201 (2005).
- [11] R. Orús, A practical introduction to tensor networks: Matrix product states and projected entangled pair states, *Annals of Physics* **349**, 117 (2014).
- [12] U. Schollwöck, The density-matrix renormalization group, *Rev. Mod. Phys.* **77**, 259 (2005).
- [13] A. Georges, G. Kotliar, W. Krauth, and M. J. Rozenberg, Dynamical mean-field theory of strongly correlated fermion systems and the limit of infinite dimensions, *Rev. Mod. Phys.* **68**, 13 (1996).
- [14] G. Carleo and M. Troyer, Solving the quantum many-body problem with artificial neural networks, *Science* **355**, 602 (2017).
- [15] H. Lange, A. Van de Walle, A. Abedinnia, and A. Bohrdt, From architectures to applications: a review of neural quantum states, *Quantum Sci. Technol.* **9**, 040501 (2024).
- [16] R. Zen, L. My, R. Tan, F. Hébert, M. Gattobigio, C. Miniatura, D. Poletti, and S. Bressan, Transfer learning for scalability of neural-network quantum states, *Physical Review E* **101**, 10.1103/physreve.101.053301 (2020).
- [17] M. Scherbela, L. Gerard, and P. Grohs, Towards a foundation model for neural network wavefunctions, arXiv preprint arXiv:2303.09949 (2023).
- [18] M. Machaczek, L. Pollet, and K. Liu, Neural quantum state study of fracton models, *SciPost Phys.* **18**, 112 (2025).
- [19] V. Hernandez, T. Spriggs, S. Khaleefah, and E. Greplova, Adiabatic fine-tuning of neural quantum states enables detection of phase transitions in weight space (2025).
- [20] A. Lucas, Ising formulations of many np problems, *Front. Phys.* **2**, 10.3389/fphy.2014.00005 (2014).
- [21] Y. Chen, T. Koch, H. Peng, and H. Zhang, Benchmarking of quantum and classical computing in large-scale dynamic portfolio optimization under market frictions, arXiv preprint arXiv:2502.05226 (2025).
- [22] T. Koch *et al.*, Quantum optimization benchmark library – the intractable decathlon, arXiv preprint arXiv:2504.03832 (2025).
- [23] T. Kadowaki and H. Nishimori, Quantum annealing in the transverse ising model, *Phys. Rev. E* **58**, 5355 (1998).
- [24] E. Farhi, J. Goldstone, S. Gutmann, and M. Sipser, Quantum computation by adiabatic evolution (2000), arXiv:quant-ph/0001106 [quant-ph].
- [25] M. Born and V. Fock, Beweis des adiabatensatzes, *Zeitschrift für Physik* **51**, 165 (1928).
- [26] T. Albash and D. A. Lidar, Adiabatic quantum computation, *Rev. Mod. Phys.* **90**, 015002 (2018).
- [27] J. Devlin, M.-W. Chang, K. Lee, and K. Toutanova, Bert: Pre-training of deep bidirectional transformers for language understanding, in *NAACL-HLT* (2019) accessed 2025-09-18.
- [28] A. Dosovitskiy, L. Beyer, A. Kolesnikov, D. Weissenborn, X. Zhai, T. Unterthiner, M. Dehghani, M. Minderer, G. Heigold, S. Gelly, J. Uszkoreit, and N. Houlsby, An image is worth 16x16 words: Transformers for image recognition at scale, arXiv:2010.11929 (2020), accessed 2025-09-18.
- [29] E. Perez, F. Strub, H. de Vries, V. Dumoulin, and A. Courville, Film: Visual reasoning with a general conditioning layer, in *Proceedings of the AAAI Conference on Artificial Intelligence* (2018) accessed 2025-09-18.
- [30] V. P. Dwivedi, L. Rampásek, M. Galkin, R. Fjeldsted, V. Krakovna, M. Brockschmidt, and X. Bresson, Graph neural networks with learnable structural and positional representations, in *ICLR* (2022) random-walk diffusion based positional encodings (RWPE/RWDIFF). Accessed 2025-09-18.
- [31] D. L. Chen *et al.*, Structure-aware transformer for graph representation learning, in *Proceedings of the 39th International Conference on Machine Learning (ICML)* (2022) uses random-walk positional encodings (RWPE). Accessed 2025-09-18.
- [32] A. Brauer, Limits for the characteristic roots of a matrix. iv: Applications to stochastic matrices, *Duke Math. J.* **19**, 75 (1952).
- [33] G. E. Santoro and E. Tosatti, Optimization using quantum mechanics: quantum annealing through adiabatic evolution, *J. Phys. A: Math. Gen.* **39**, R393 (2006).
- [34] J. J. Sakurai and J. Napolitano, *Modern Quantum Mechanics* (Cambridge University Press, 2020).